Conductance Through a Bent Carbon Nanotube

Mathias Dyrberg Loft

Bachelor Thesis

Supervisor: Karsten Flensberg

Spring 2010
University of Copenhagen

1 Resumé

I dette Bachelorprojekt udledes et teoretisk udtryk for konduktansen gennem et bøjet carbon nanorør. Udgangspunktet for studiet af carbon nanorør er grafen, der kan beskrives ved to undergitre bestående af A og B carbonatomer, som definerer AB-underrummet. Ved hjælp af en tight-binding model opstillede vi en approksimativ Hamiltonoperator og tilhørende energi dispersion for grafen i nærheden af $\mathbf{K}(\mathbf{K'})$-punkterne, der er defineret som hjørnerne i den hexagonale første Brillouin zone. Ved brug af periodiske randbetingelser og Blochs theorem udvidedes billedet til carbon nanorør, der er dannet ved at rulle et grapfenlag sammen til en cylinder, således at en kvasi 1D-dispersion opnås.

Systemet udvikledes yderligere ved inkorporation af en række perturbationer. Vi fandt at et magnetfelt inducerede båndgab for metalliske nanorør samt brydning af $\mathbf{K}(\mathbf{K'})$-udartningen for halvledende rør. Spin-bane koblingen og hybridisering mellem π og σ båndene pga. nanorøret krumning ledte yderligere til en asymmetrisk splitning af Kramer doubletterne, der består af hhv. $\mathbf{K}(\mathbf{K'})\uparrow(\downarrow)$ og $\mathbf{K}(\mathbf{K'})\downarrow(\uparrow)$, hvor pilene indikerer spinpolarisering langs med røret, i lednings- og valensbåndet. Ved at medtage mixing af $\mathbf{K}$ og $\mathbf{K'}$ – der opstår pga. vekselvirkninger med omgivelserne, som bryder rotations symmetrien – blev det samlede resultat en fuldstændig opslitning af de ellers fire-dobbelt udartede energibånd. De tilhørende eigenfunktioner bestod af linear kombinationer af alle de otte basis vektorer, der udspænder det otte-dimensionelle Hilbert rum, som følger af de tre 2-dimensionelle underrum AB, $\mathbf{K}(\mathbf{K'})$ og spin.

Vi inkorporerde en translationel bøjning af røret ved at projicere Hamiltonoperatoren over i et lokalt koordinatsystem i det bøjede rør i et segment, der antoges at være lige. Dernæst udarbejdede vi et udtryk til sammensætning af bølgefunktionerne på hver side af bøjningen, hvor røret antoges at være uendeligt langt så ikke-propagerende løsninger kunne negligeres. Dette muliggjorde konstruktionen af spredningsmatricen, der relaterer ind- og udgående bølger. Herudfra bestemtes transmissions- og reflektionskoefficienterne, så et udtryk for konduktansen ved brug af Landauer formlen kunne bestemmes.

Simuleringer af konduktansen for forskellige nanorørkonfigurationer som funktion af fermienergien blev udført ved brug af et selvkonstrueret MATLAB script, i hvilket forskellige parametre blev varieret. Nogle af simuleringerne var plaget af ufysiske fluktuationer i transmissionen (konduktansen), som må tilskrives begrænsninger i koden. Vi var dog i stand til at udføre simuleringer for nogle typer nanorørkonfigurationer, der indikerede en række spændende fænomener. Bl.a. så vi kvantisering af konduktansen i enheder af konduktanskvaten e^2/h, der øgedes i heltallige trin heraf, efterhånden som fermienergien førøgedes; en effekt der tidligere er beskrevet eksperimentelt. Yderligere så vi for visse typer nanorørsbøjninger en indikation på resonant tunnelering. De numeriske vanskeligheder taler dog for at en udvikling af koden er nødvendig. Bachelorprojektet har dog en endelig længde, og denne udvikling må derfor følge i et senere projekt.

Gennem arbejdet med projektet har jeg opnået en markant større indsigt i carbon nanorørsfysikken. Rejsen hertil har lang og til tider frustrerende. I den forbindelse vil jeg gerne rette en stor tak til min vejleder Karsten Flensberg for at kunne lede mig på rette spor. Jeg skylder også en stor tak til de øvrige medlemmer af nano-teori gruppen. Især til Stephan Weiss og Frederik Treue. En særlig tak skal også lyde til Morten Kjærgaard for utrættelig faglig og moralsk opbakning foruden frugtbare diskussioner og et par skarpe øjne i retteprocessen.

Mathias Dyrberg Loft

Maj 2010, København

Abstract

In this thesis a theoretical expression for the conductance through a bent nanotube is derived. The idea is inspired by a recent work by K. Flensberg and C. Markus, in which bent nanotubes are shown to be a prominent candidate for qubit realization [1]. An approximate Hamiltonian for graphene in the vicinity of the high-symmetry $\mathbf{K}(\mathbf{K}')$-points is developed from the tight-binding model. An extension to carbon nanotubes, which are constructed from rolling up a graphene layer, is done using periodic boundary conditions. In addition, various perturbations are taken into account: the effect of a magnetic field, spin-orbit coupling, curvature induced hybridization and $\mathbf{K}(\mathbf{K}')$-mixing. As a result, the energy bands split and the eigenstates become mixed. Assuming the tube to be locally straight, a bending in the translational direction is included through projection on to the local coordinate system of the tube segment. An integration routine for connecting the wavefunctions in the beginning and end of the tube is developed, such that a scattering matrix can be constructed, from which the transmission and reflection are deduced. From the Landauer formula the conductance can thus be determined. Using MATLAB, simulations of the transmission (conductance) as a function of the Fermi energy were performed for various tube geometries. Some of the simulations were haunted by unphysical fluctuations in the transmission and reflection which needs to addressed in a future study. However results indicating experimentally reported ballistic transport in nanotubes and quantized conductance steps in e^2/h due to the energy splitting were observed. In addition, we found indication of resonance tunneling in certain nanotube geometries.

Contents

2 Introduction

Ever since carbon nanotubes (CNT) were discovered by Sumio Iijima in 1991 [2] they have undergone intense theoretical and experimental study. Hundreds of papers in which electronic transport properties of nanotubes are studied have been published, showing very large mean free paths and quantized conductance e.g. [3, 4]. Recent experiments have shown that the effect of spin-orbit coupling in CNTs, which was at first thought to be negligible, should also be included when studying ultra clean nanotubes [5]. Various theoretical studies have contributed to the construction of an effective Hamiltonian including spin-orbit coupling on the basis of the tight-binding Hamiltonian of graphene [6], showing breaking of the energy degeneracy yielding Kramer doublets. Further, the introduction of a magnetic field has been shown to induce spin-splitting and breaking of the degeneracy of the $\mathbf{K}(\mathbf{K'})$-points due to the Aharonov-Bohm effect [7]. Including the finite curvature of the nanotube surface an elaborate effective Hamiltonian has been developed [8, 9, 10]. The inclusion of the perturbations is important when making energy band calculations.

Although many different types of conductance measurements have been performed, few have focused on bent nanotubes, however some experimental data are available e.g. [11]. The bent tubes have theoretically been shown to be a prominent candidate for qubit realization via quantum dots [1]. Therefore it is natural to investigate their electronic properties in greater detail. In this thesis we develop a theoretical expression for the conductance through a bent nanotube including the effects of spin-orbit and curvature. To our knowledge this has not been done before.

We start out by examining the graphene and carbon nanotube physics and develop an effective Hamiltonian for the unperturbed system following a well described procedure [12, 13]. The derivations involve many lengthy calculations, which have been omitted in the main text. The interested reader should refer to the appendices for a detailed assessment. We then take the above perturbations into consideration, and following the methods in [1] we derive an expression for the Hamiltonian of a bent nanotube as a function of the bending angle.

From the Hamiltonian a routine for integrating the wavefunction along the tube is established, thereby enabling the construction of the scattering matrix from which the transmission and reflection are deduced. From the Landauer formula a theoretical expression for the conductance follows. We end this theoretical assessment by simulating and analyzing the conductance of various bent nanotube geometries.

3 Elements of Carbon Nanotube Physics

In this section the preliminaries of carbon nanotube physics are established. We start out by defining the relevant geometries for graphene and carbon nanotubes. We then derive the dispersion relation and effective Hamiltonian for graphene (See Appendix A) followed by an extension to carbon nanotubes by use of periodic boundary conditions.

3.1 Graphene

Graphene consists of a single layer of graphite, which is constructed in a hexagonal (honeycomb) lattice with a carbon atom on each lattice site as illustrated in Figure 3.1 **(a)**. The distance between two neighboring carbon atoms is $a_{\text{c-c}} = 1.42\text{Å}$ and the lattice constant is $a = 2.46$ Å[13]. In addition to the two tightly bound $1s$ core electrons, carbon has a valency

of four, three of which are allocated to form the in-graphene-plane sp-2 hybridized σ-bond. This leaves one electron to occupy the perpendicular p_z orbital, leading to the formation of the bonding π-band and anti-bonding π^*-band. The hexagonal geometry requires a unit cell consisting of at least two atoms; one possible choice of lattice vectors spanning a diatomic unit cell are the non-orthogonal vectors [13, p. 25]

$$\mathbf{a}_1 = \frac{a}{2} \begin{pmatrix} \sqrt{3} \\ -1 \end{pmatrix} \text{ and } \mathbf{a}_2 = \frac{a}{2} \begin{pmatrix} \sqrt{3} \\ 1 \end{pmatrix}. \tag{3.1}$$

The two carbon atoms in the unit cell are conventionally labeled A and B, as illustrated in Figure 3.1 **(a)**. With $\mathbf{d} = \mathbf{R}_B - \mathbf{R}_A$ connecting the two atoms, the honeycomb lattice can be spanned by two equivalent sublattices consisting of only A and B atoms, which are situated at

$$\mathbf{R}_A = u_1\mathbf{a}_1 + u_2\mathbf{a}_2 \text{ and } \mathbf{R}_B = u_1\mathbf{a}_1 + u_2\mathbf{a}_2 + \mathbf{d}, \tag{3.2}$$

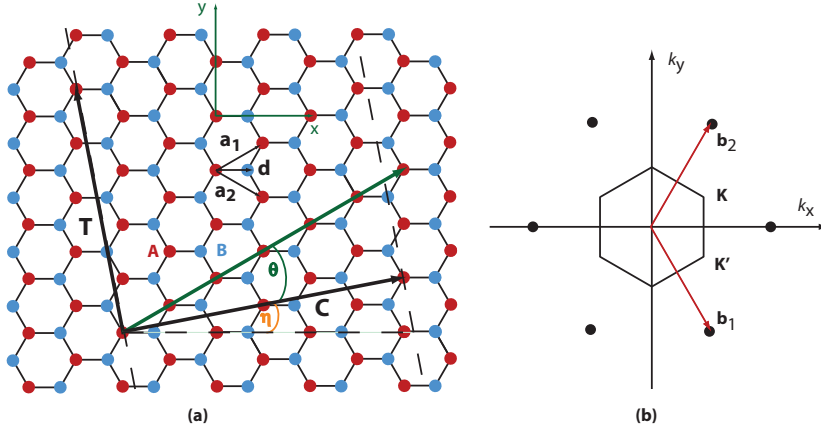where $(u_1, u_2 \in \mathbb{Z})$. The reciprocal lattice vectors for graphene are constructed from the

Figure 3.1: **(a)** The hexagonal graphene lattice along with the two lattice vectors $\mathbf{a}_1$ and $\mathbf{a}_2$. The chiral vector $\mathbf{C}$ and the translational vector $\mathbf{T}$ of the carbon nanotubes are also indicated along with the chiral angle θ. η is the angle between $\mathbf{C}$ and $\hat{x}$. **(b)** The hexagonal FBZ of graphene along with the indication of the $\mathbf{K}$ and $\mathbf{K}'$ points and the reciprocal lattice vectors given in red.

condition $\mathbf{b}_i \cdot \mathbf{a}_j = 2\pi\delta_{ij}$ [14, p. 29] and are found to be

$$\mathbf{b}_1 = \frac{2\pi}{a} \begin{pmatrix} \frac{1}{\sqrt{3}} \\ -1 \end{pmatrix} \text{ and } \mathbf{b}_2 = \frac{2\pi}{a} \begin{pmatrix} \frac{1}{\sqrt{3}} \\ 1 \end{pmatrix}. \tag{3.3}$$

The First Brillouin Zone (FBZ) is defined as the volume enclosed by the planes perpendicular to the bisectors of the reciprocal lattice vectors [14, p. 34]. As seen in Figure 3.1 **(b)** the FBZ also constitutes a honeycomb lattice.

As will be clear in what follows, the $\mathbf{K}$ and $\mathbf{K}'$ points – which are defined as the two inequivalent corners of the FBZ – play a very important role in graphene and carbon nanotube physics, as they constitute the points at which the energetic distance between the π and π^*-band is at a minimum. In Figure 3.1 **(b)** the $\mathbf{K}$ and $\mathbf{K}'$ points are given as

$$\mathbf{K} = \frac{2\pi}{a} \begin{pmatrix} \frac{1}{\sqrt{3}} \\ \frac{1}{3} \end{pmatrix} \text{ and } \mathbf{K}' = \frac{2\pi}{a} \begin{pmatrix} \frac{1}{\sqrt{3}} \\ -\frac{1}{3} \end{pmatrix}. \tag{3.4}$$

The remaining corners are equivalent to $\mathbf{K}$ and $\mathbf{K}'$, since they are connected by reciprocal lattice vectors and therefore cannot be identified as unique wavevectors.

3.2 Carbon Nanotubes

A carbon nanotube is constructed by folding a graphene sheet into a hollow cylindrical tube. This can of course be done in many ways, and it turns out that the folding determines whether the tube is metallic or semi-conducting. The individual CNTs are uniquely characterized by the chiral vector which is defined

$$\mathbf{C} = n_1\mathbf{a}_1 + n_2\mathbf{a}_2 \tag{3.5}$$

where $n_1, n_2 \in \mathbb{Z}$ and $n_2 \leq n_1$ to avoid degeneracy. The name is motivated by the observation that for certain integer pairs, (n_1, n_1) and $(n_1, 0)$, we get *achiral* nanotubes, meaning that they have a mirror image with identical structure. The conformations are called *armchair* and *zig-zag*, respectively. For any other conformation, however, the tubes are *chiral*, i.e. there is no symmetry plane [13]. Every essential geometric feature of the nanotube may be derived from the chiral vector.

E.g., the radius is determined by taking the length of the chiral vector divided by 2π, yielding

$$R = \frac{|\mathbf{C}|}{2\pi} = \frac{a\sqrt{n_1^2 + n_2^2 + n_1 n_2}}{2\pi} \tag{3.6}$$

since $|\mathbf{a}_1| = |\mathbf{a}_2| = a$ and $\mathbf{a}_1 \cdot \mathbf{a}_2 = \frac{a^2}{2}$. In addition, the *chiral angle* θ is defined as the angle between the chiral vector and $\boldsymbol{a}_1$. For armchair and zig-zag nanotubes it corresponds to $\theta = 30^\text{o}$ and $\theta = 0$, respectively. In general is it found from the equation

$$\cos\theta = \frac{\mathbf{C} \cdot \mathbf{a}_1}{|\mathbf{C}||\mathbf{a}_1|} = \frac{2n_1 + n_2}{2\sqrt{n_1^2 + n_2^2 + n_1 n_2}}. \tag{3.7}$$

The translation vector is defined as the unit vector of the 1-D nanotube, i.e. it is the direction and length one has to move through the nanotube before it starts to repeat itself. It is parallel to the tube axis and perpendicular to the chiral vector and can be expressed in terms of $\mathbf{a}_1$ and $\mathbf{a}_2$ as follows

$$\mathbf{T} = t_1\mathbf{a}_1 + t_2\mathbf{a}_2.$$

By definition, the unit cell has to be as small as possible, meaning that we are to choose the smallest possible integers t_1 and t_2. From the requirement $\mathbf{C} \cdot \mathbf{T} = 0$ we have that $0 = (t_1(2n_1 + n_2) + t_2(2n_2 + n_1))$ which has the (minimal) solution

$$t_1 = \frac{2n_1 + n_1}{d_R}, \quad t_2 = -\frac{2n_1 + n_2}{d_R}, \tag{3.8}$$

where d_R is the greatest common deviser (*gcd*) of $(2n_2 + n_1)$ and $(n_1 + 2n_2)$. In Figure 3.1 **(a)** an example of a (4,2)-folded nanotube is illustrated, along with the chiral vector, the chiral angle and the translational vector.

It is clear that the CNT unit cell contains more atoms than the diatomic unit cell of graphene. The precise number is found by first determining the number of graphene unit cells within the larger CNT unit cell, which is done by dividing the volume of the two:

$$N = \frac{|\mathbf{C} \times \mathbf{T}|}{|\mathbf{a}_1 \times \mathbf{a}_2|} = \frac{2(n_2^2 + n_1^2 + n_1 n_2)}{d_R}. \tag{3.9}$$

Remembering that each unit cell contains two atoms, a total of $2N$ carbon atoms, or equivalently $2N$ p_z orbitals, are contained within the CNT unit cell. Thus including spin, we have a total of $4N$ possible states.

As a conclusion of this section, the reciprocal lattice vectors of the CNT are stated. Since the unit cell vectors are orthogonal, so are the reciprocal lattice vectors, i.e. they will be in the direction of $\mathbf{C}$ and $\mathbf{T}$. The vectors are derived from the conditions $\mathbf{Q_C} \cdot \mathbf{T} = \mathbf{Q_T} \cdot \mathbf{C} = 2\pi$ and $\mathbf{Q_C} \cdot \mathbf{C} = \mathbf{Q_T} \cdot \mathbf{T} = 0$ and are found to be

$$\mathbf{Q_C} = \frac{1}{N}(-t_2\mathbf{b}_1 + t_1\mathbf{b}_2), \quad \mathbf{Q_T} = \frac{1}{N}(n_2\mathbf{b}_1 - n_1\mathbf{b}_1), \tag{3.10}$$

where N is determined from eq. (3.9) and $\mathbf{b}_1$ and $\mathbf{b}_2$ are the reciprocal lattice vectors of graphene from eq. (3.3). Due to the folding of the graphene layer, the reciprocal vectors along the circumferential direction become quantized, resulting in a 1-D band structure. This phenomenon is treated in great detail, when we develop the dispersion relation for carbon nanotubes.

3.3 Energy dispersion for graphene

The $2p_z$-orbitals are the main contributers to the electronic transport in graphene. This allows us to investigate the energy dispersion through a tight-binding scheme in which we only focus on the π-band.

In Appendix A a thorough derivation of the energy dispersion for graphene is given. It relies primarily on Bloch's theorem and construction of a total wavefunction from linear combinations of the perpendicular atomic p_z orbitals from the two sublattices A and B. The rest of derivation amounts to solving the Schrödinger equation within this subset. It turns out that the energy dispersion equals the Fermi energy – which is set as the zero of energy – for $\mathbf{k} = \mathbf{K}(\mathbf{K}')$. Since only electrons in the vicinity of the Fermi-energy contribute to electronic transport, the dispersion relation is expanded in this region. The formal expansion to first order can be found in Appendix B and yields the Hamiltonian

$$\mathcal{H} = \hbar v_F \begin{pmatrix} 0 & i\kappa_x + \tau_3\kappa_y \\ -i\kappa_x + \tau_3\kappa_y & 0 \end{pmatrix}, \tag{3.11}$$

where $\tau_3 = 1(-1)$ for $\mathbf{K}(\mathbf{K}')$ and $\boldsymbol{\kappa} = (\kappa_x, \kappa_y)$ is the wavevector expanded around the $\mathbf{K}(\mathbf{K}')$-points. This gives an expression for the energy dispersion and eigenfunctions in the vicinity of these high-symmetry points:

$$\epsilon_\pm(\boldsymbol{\kappa}) = \pm\hbar v_F|\boldsymbol{\kappa}|, \quad \begin{pmatrix} \alpha \\ \beta \end{pmatrix}_\pm = \frac{1}{\sqrt{2}}\begin{pmatrix} \mp e^{i\beta} \\ 1 \end{pmatrix}, \tag{3.12}$$

where $\beta = \arg(\boldsymbol{\alpha}(\mathbf{k}))$ with $\boldsymbol{\alpha}(\boldsymbol{k})$ defined in eq. (A.8). We now turn to the – for this thesis – more interesting case of the energy bands of carbon nanotubes which will be the topic of the remainder of this section.

3.4 Energy dispersion for carbon nanotubes

The folding of a graphene sheet into a cylindrical carbon nanotube requires that $\psi_{\mathbf{k}}(\mathbf{r} + \mathbf{C}) = \psi_{\mathbf{k}}(\mathbf{r})$ since the wavefunction has to be continuous in the circumferential direction. This results in a quantization condition on the circumferential component of the wavevector, while the translational component remains practically continuous for long nanotubes[1]. The

---

[1] With a finite CNT length L, the vectors are discrete in steps of $\delta k = 2\pi/L$, so for long tubes ($\approx \mu$m) compared to a CNT circumference of the order nm continuity can be assumed.
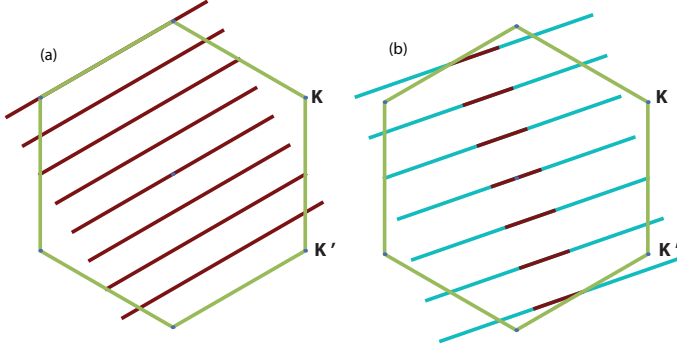
Figure 3.2: The FBZ of graphene (green) with indication of the $\mathbf{K}$ and $\mathbf{K'}$ points and with **(a)** the FBZ of a (4,4)-armchair CNT and **(b)** (4,2)-chiral CNT superimposed (red lines). $N = 8$ and $N = 28$, respectively, such that there are 8 and 28 unique wavevectors each of length $2\pi/|\mathbf{T}|$. (In **(b)** only the seven lying within the FBZ of graphene are shown. The blue lines indicate the extended zone scheme). For the armchair tube, the wavevectors touch the K points while this is not the case for the chiral tube.

quantization condition can be derived from the Bloch Theorem [15, p. 157],

$$\psi_{\mathbf{k}}(\mathbf{r} + \mathbf{C}) = e^{i\mathbf{k}\cdot\mathbf{C}}\psi_{\mathbf{k}}(\mathbf{r}) = \psi_{\mathbf{k}}(\mathbf{r}), \tag{3.13}$$

which leads to the result

$$\mathbf{k} \cdot \mathbf{C} = 2\pi n, \tag{3.14}$$

where $n \in \mathbb{Z}$. Decomposing the wavevector into a component parallel to the tube axis ($\mathbf{k}_T$) and one perpendicular to it ($\mathbf{k}_C$), such that

$$\mathbf{k} = \mathbf{k}_C + \mathbf{k}_T = k_C \frac{\mathbf{C}}{|\mathbf{C}|} + k_T \frac{\mathbf{T}}{|\mathbf{T}|}, \tag{3.15}$$

we get the condition $k_C = \frac{2\pi}{|\mathbf{C}|}n$, since $\mathbf{C} \cdot \mathbf{T} = 0$ per definition. The circumference of the nanotube is small compared to the length of the tube, hence the k_C vectors split up and the 2-D graphene bandstructure turns into 1-D subbands labeled by n.

From eq. (3.10) we have the condition on the reciprocal CNT lattice vector $N\mathbf{Q}_C = -t_2\mathbf{b}_1 + t_1\mathbf{b}_2$, where N is the number of graphene unit cells within the CNT unit cell eq. (3.9). With $\mathbf{b}_1$ and $\mathbf{b}_2$ defined as reciprocal vectors of graphene, $N\mathbf{Q}_C$ also corresponds to a reciprocal lattice vector of 2-D graphene, such that two wavevectors which differ by $N\mathbf{Q}_C$ are equivalent. Since t_1 and t_2 have no common denominator other than unity, none of the $\mu\mathbf{Q}_C$ vectors ($\mu \in \{1, 2, \ldots, N-1\}$) are reciprocal lattice vectors of graphene; we thus have N discrete k_C vectors for $n \in \{0, 1, 2, \ldots, N-1\}$.

The perpendicular bisection of the CNT reciprocal lattice vector in the translational direction have the length $\pi/|\mathbf{T}|$, such that the FBZ is defined by $\frac{-\pi}{|\mathbf{T}|} \leq k_T \leq \frac{\pi}{|\mathbf{T}|}$, with k_T being practically continuous, and the N discretized k_C, which are spaced by $2\pi/|\mathbf{C}|$. In Figure 3.2 the discretization is demonstrated in the reduced zone scheme (red) and extended zone scheme (blue) of the FBZ of the CNT for two different geometries; **(a)** an armchair (4,4)-tube and **(b)** a chiral (4,2)-tube. For the armchair tube $N = 8$, i.e. there are 8 unique wavevectors which all lie within the FBZ of graphene. For the chiral tube, $N = 28$ yielding 28 unique vectors, but only the ones lying within the FBZ of graphene are shown. An example of the dispersion relation for the (4,4)-armchair tube is given in Figure A.1 **(b)** in Appendix A showing eight conductance and eight valence bands since $N = 8$.

3.4.1   Carbon nanotube physics in the vicinity of the Fermi energy

In order to determine the approximate Hamiltonian for CNTs around the $\mathbf{K}(\mathbf{K'})$-points, the expansion in $\boldsymbol{\kappa}$ at the Fermi energy for graphene eq. (3.11) must be transformed into the CNT coordinate system spanned by the orthogonal basis $\left(\frac{\mathbf{T}}{|\mathbf{T}|}, \frac{\mathbf{C}}{|\mathbf{C}|}\right)$. In Appendix C it is shown that the Hamiltonian in the reference frame of the carbon nanotube is given

$$\mathcal{H}_0 = \hbar v_F \begin{pmatrix} 0 & i\kappa_C + \tau_3 \kappa_T \\ -i\kappa_C + \tau_3 \kappa_T & 0 \end{pmatrix} \qquad (3.16)$$

As for κ_y, the translational vector component κ_T is again continuous, whereas the discretization of κ_C may be found from the quantization condition in eq. (3.14) yielding (see Appendix C for details)

$$\kappa_C = \frac{1}{R}\left(m - \frac{\tau_3 \mu}{3}\right), \qquad (3.17)$$

where μ is determined from $(n_2 - n_1) = 3N + \mu$ $(N \in \mathbb{Z})$. I.e. for $(n_2 - n_1)/3 \in \mathbb{Z}$, $\mu = 0$, and $\mu = \pm 1$ for $(n_2 - n_1)/3 \notin \mathbb{Z}$ in which case the latter term is not an integer. The energy dispersion within the the $\mathbf{K}(\mathbf{K'})$ expansion is found from the Hamiltonian in eq. (3.16) and becomes

$$\epsilon(\kappa) \rightarrow \epsilon_m(k_T) = \pm \hbar v_F \sqrt{\kappa_C^2 + \kappa_T^2}. \qquad (3.18)$$

Hence for a carbon nanotube to be gapless, i.e. be metallic, $\mu = 0$. If $\mu = \pm 1$ there will be a gap between the conduction and valence bands, since we may not choose an m such that $\kappa_C = 0$.

In Figure 3.3 the dispersion relations of the lowest lying energy band – corresponding to the κ_C being closest to the $\mathbf{K}(\mathbf{K'})$-points – are shown for **(a)** metallic $(4,4)$-armchair tube $(\mu = 0)$ and **(b)** a semiconducting, chiral $(4,2)$-tube$(\mu = -1)$. The dispersion relation of the armchair tube forms the characteristic Dirac-cone, and the conduction and valence band touch at $\kappa_y = 0$, i.e. at the $\mathbf{K}(\mathbf{K'})$ point. The chiral tube has a bandgap.

The conditions for a CNT to be metallic or semiconducting corresponds to whether the wavevector touch the $\mathbf{K}(\mathbf{K'})$ points or not. This is illustrated for the two CNTs in Figure 3.2. In the case of the armchair tube one of the wavevectors touch and the tube is metallic. However, none of the wavevectors of the chiral tube touch the $\mathbf{K}(\mathbf{K'})$-points. We are thus unable to choose a m and κ_T such that the energy of the conduction and valence band match. It will be shown later that due to perturbations, even metallic tubes will under some circumstances become semiconducting.

3.5   Subspaces

The Hamiltonian for the CNTs in eq. (3.16) is a 2×2-matrix, when keeping τ_3 as an entry. This 2×2 systems constitutes the AB-subspace, as illustrated in the diagram below. Each entry corresponds to the weight of the atomic orbitals on the A and B sublattice and the mixing between these:

$$\mathcal{H}_0 \sim \left(\begin{array}{c|c} AA & AB \\ \hline BA & BB \end{array}\right). \qquad (3.19)$$

Since the Hamiltonian has off-diagonal elements there is a mixing of the p_z-orbitals from A and B atoms, which follows from making linear combinations of orbitals from atoms on different
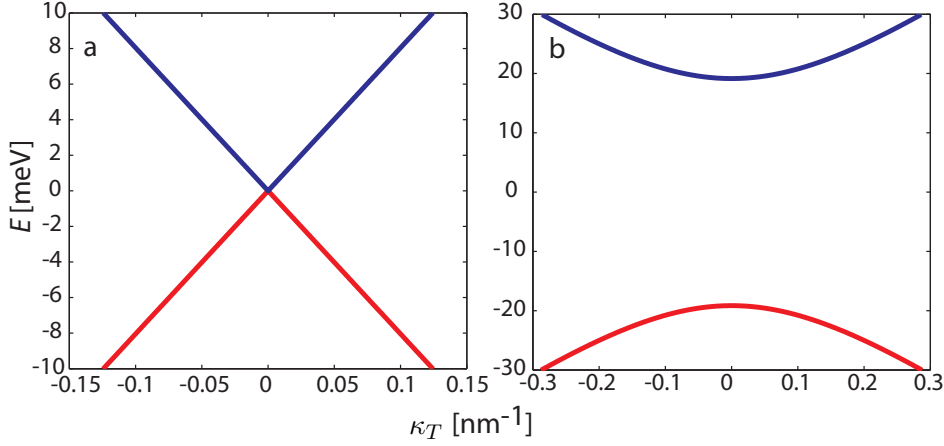
Figure 3.3: Energy dispersion expanded around the $\mathbf{K}(\mathbf{K}')$-points for the lowest lying energy band. **(a)** (4,4)-armchair tube with no external interactions. The conductance and valence band meet at $\kappa_y = 0$, hence the tube is metallic. **(b)** (4,2)-chiral tube corresponding to $\mu = -1$. An energy gap is present due to the periodic boundary conditions, hence the tube is semi-conducting.

sublattices. Inserting $\tau_3 = 1(-1)$ for $\mathbf{K}(\mathbf{K}')$, the subspace is expanded into a 4×4-matrix in which each quadrant corresponds to $\mathbf{K}\mathbf{K}$, $\mathbf{K}\mathbf{K}'$ $\mathbf{K}'\mathbf{K}$ and $\mathbf{K}'\mathbf{K}'$, i.e.

$$\mathcal{H}_0 = \hbar v_F \begin{pmatrix} 0 & -i\kappa_C + \kappa_T & 0 & 0 \\ i\kappa_C + \kappa_T & 0 & 0 & 0 \\ 0 & 0 & 0 & -i\kappa_C - \kappa_T \\ 0 & 0 & i\kappa_C - \kappa_T & 0 \end{pmatrix} \sim \left(\begin{array}{c|c} \mathbf{K}\mathbf{K} & \mathbf{K}\mathbf{K}' \\ \hline \mathbf{K}'\mathbf{K} & \mathbf{K}'\mathbf{K}' \end{array} \right). \quad (3.20)$$

Each of the quadrants then corresponds to an AB-subspace as indicated by the coloring. The Hamiltonian is diagonal in $\mathbf{K}\mathbf{K}'$-space, i.e. there is no mixing between the $\mathbf{K}$ and $\mathbf{K}'$ points.

In addition, electrons also have a spin degree of freedom, such that an additional subspace is needed. With all subspaces being 2×2 dimensional, we may use the *Pauli spin matrices* as a basis since they form a complete set. The spin matrices are denoted σ_i, τ_i, S_i, $i \in \{1, 2, 3\}$ and $\boldsymbol{\sigma}, \boldsymbol{\tau}, \boldsymbol{S}$ are the matrices containing the corresponding 2×2-matrices as entries. The matrices span, respectively, the AB-subspace the $\mathbf{K}\mathbf{K}'$-subspace, also called *valley-space*, and the spin-subspace. We take the spin space to be the inner subspace, such that each quadrant in the AB-subspace is further expanded into a 2×2 spin-subspace. In this language we may write the Hamiltonian eq. (3.20) very neatly

$$\mathcal{H} = \hbar v_F (\tau_0 \sigma_2 S_0 \kappa_C + \tau_3 \sigma_1 S_0 \kappa_T), \quad (3.21)$$

where τ_0, σ_0, S_0 denote the identities in the relevant subspace.

The formal multiplication of subspace matrices corresponds to outer products, in the sense that they operate only upon the subspace in question, leaving the others untouched. Therefore we should write $\otimes$ in between the matrices, but this notation is clumsy so we refrain from doing so. Since each of the subspaces is 2×2, the total Hilbert space is 8×8 and is spanned by the eight-dimensional basis which – with the given order of the subspaces – becomes

$$
\begin{pmatrix}1\\0\\0\\0\\0\\0\\0\\0\end{pmatrix}_{\sim KA\uparrow}
\begin{pmatrix}0\\1\\0\\0\\0\\0\\0\\0\end{pmatrix}_{\sim KA\downarrow}
\begin{pmatrix}0\\0\\1\\0\\0\\0\\0\\0\end{pmatrix}_{\sim KB\uparrow}
\begin{pmatrix}0\\0\\0\\1\\0\\0\\0\\0\end{pmatrix}_{\sim KB\downarrow}
\begin{pmatrix}0\\0\\0\\0\\1\\0\\0\\0\end{pmatrix}_{\sim K'A\uparrow}
\begin{pmatrix}0\\0\\0\\0\\0\\1\\0\\0\end{pmatrix}_{\sim K'A\downarrow}
\begin{pmatrix}0\\0\\0\\0\\0\\0\\1\\0\end{pmatrix}_{\sim K'B\uparrow}
\begin{pmatrix}0\\0\\0\\0\\0\\0\\0\\1\end{pmatrix}_{\sim K'B\downarrow}
$$

$$(3.22)$$

The basis vectors $\{|\tau,\sigma,S\rangle\}$ are denoted by the quantum numbers $\tau = 1(-1)$ for $\mathbf{K}(\mathbf{K}')$ $\sigma = 1(-1)$ for $A(B)$ and $S = 1(-1)$ for $\uparrow(\downarrow)$. E.g. $|1,-1,-1\rangle$ corresponds to the basis vector $KB\downarrow$. This will be the basis of choice in the remainder of this thesis.

The states in the valence and conduction bands, respectively, are four-fold degenerate for unperturbed nanotubes. When applying a magnetic field and taking into account spin-orbit couplings and curvature the energy bands will split up. This is the topic of the next section.

4 Carbon Nanotube Perturbations

The derivation of the Hamiltonian and the corresponding eigenenergies and eigenfunctions has so far been for infinitely straight and completely isolated nanotubes, in which we have neglected any possible interactions with the environment. We now turn to the daunting task of expanding this simple picture to one involving various perturbations of the nanotube. The first step is to study the effect of placing it in a magnetic field.

4.1 Carbon nanotubes in a magnetic field

The magnetic field couples to both the spin and the orbital motion. Introducing a magnetic field amounts to a change of the canonical momentum, $\mathbf{p} \rightarrow \mathbf{p} + e\mathbf{A}$, where $\mathbf{A}$ is the magnetic vector potential such that $\mathbf{B} = \boldsymbol{\nabla} \times \mathbf{A}$. In general, the Schrödinger equation thus reads

$$\frac{1}{2m}\left[\frac{\hbar}{i}\boldsymbol{\nabla} + e\mathbf{A}\right]^2 \psi = \epsilon\psi. \tag{4.1}$$

Assuming the magnetic field points in the direction of the tube, the magnetic flux through it becomes

$$\Phi = \int dr^2 B = \int d\mathbf{a} \cdot (\nabla \times \mathbf{A}) = \oint d\mathbf{l} \cdot \mathbf{A}, \tag{4.2}$$

upon invoking Stokes Theorem. With these conditions the vector potential points in the direction of the tube circumference such that in cylindrical coordinates

$$\mathbf{A} = \frac{\Phi}{2\pi r}\boldsymbol{\phi}. \tag{4.3}$$

The solutions to the Schrödringer equation (4.1) now take the form [15, p.724]

$$\psi \propto \exp\left[i\mathbf{k}\cdot\mathbf{r} + i\frac{e}{\hbar}\int^{\mathbf{r}} d\mathbf{r}' \cdot \mathbf{A}(\mathbf{r}')\right], \tag{4.4}$$

which can be seen by insertion into eq. (4.1). Since $\nabla \cdot \mathbf{A} = 0$ (from eq. (4.3)), applying the Hamiltonian leads to the following

$$\begin{aligned}
\mathcal{H}\psi &= \frac{1}{2m}\left[-\hbar^2\nabla^2 - 2i\hbar e\mathbf{A}\cdot\boldsymbol{\nabla} + e^2A^2\right]\psi \\
&= \frac{1}{2m}\left[\hbar^2\left(\mathbf{k}+\frac{e}{\hbar}\mathbf{A}\right)^2 - 2\hbar e\mathbf{A}\cdot\left(\mathbf{k}+\frac{e}{\hbar}\mathbf{A}\right) + \left(\frac{e\Phi}{2\pi R}\right)^2\right]\psi;
\end{aligned} \qquad (4.5)$$

confirming that it is indeed a solution. As a consequence, electrons traveling a complete circuit acquire an extra phase of $\frac{\Phi e}{\hbar}$ where the flux through the tube is $\Phi = B\pi R^2$, since with $r = R$ we get

$$i\frac{e}{\hbar}\int^{\mathbf{r}} d\mathbf{r}' \cdot \mathbf{A}(\mathbf{r}') = i\frac{e}{\hbar}\int_0^{2\pi} Rd\phi\frac{\Phi}{2\pi R} = i2\pi\frac{e}{h}\Phi \qquad (4.6)$$

This effect is credited to *Aharonov* and *Bohm*. The effect in nanotubes is thus expressed through a change in the periodic boundary conditions [12],

$$\psi(\mathbf{r}+\mathbf{C}) = \psi(\mathbf{r})\exp(i2\pi\frac{e}{h}\Phi), \qquad (4.7)$$

leading to a change in the circumferential quantum number determined from eq. (3.17)

$$\kappa_C = \left(m + \frac{\Phi}{\Phi_0} - \frac{\tau_3\mu}{3}\right)/R, \qquad (4.8)$$

where $\Phi_0 = \frac{h}{e}$ is the flux quantum. It can be shown that the magnetic field for all practical purposes only couples to the circumferential component of the momentum [1, Methods] in nanotubes, such that even when the magnetic field is not aligned parallel to the tube, only the circumferential component is affected.

In addition, the magnetic field also couples to the spin degree of freedom, exerting a torque on the spin [16, p. 179]

$$\mathcal{H}_Z = \mu_S\tau_0\sigma_0\mathbf{B}\cdot\mathbf{S} \qquad (4.9)$$

where $\mu_S = \frac{1}{2}g_s\mu_B$ and $\mathbf{S}$ being the Pauli spin matrices in spin-space with eigenvalues ± 1. The Z refers to the *Zeeman splitting* of the energies. The effects of the magnetic field for the lowest lying energy level is thus: 1) to induce a gap in the energy spectrum (even in the case of metallic tubes) and 2) for semiconducting tubes, to induce $\mathbf{K}(\mathbf{K}')$-degeneracy breaking; in both cases due to the Aharonov-Bohm effect on the circumferential quantization. And finally, 3) to induce a splitting of the energies of different spin directions (up and down along the tube). The effect is illustrated for a magnetic field of 4 T aligned parallel to the tube in Figure 4.1, with **(a)** and **(b)** corresponding to the (4,4)-armchair and (4,2)-chiral tubes which were shown without a magnetic field in Figure 3.3.

4.2 Spin-orbit coupling and curvature induced $\sigma - \pi$–hybridization

Additional perturbations of the nanotube arise from two sources: 1) The spin-orbit-coupling, which as the name suggest couples the orbital momentum and spin, leading to $\sigma - \pi$–orbital hopping and 2) curvature induced hybridizations. This effect occurs because the configuration of the orbitals change due to the finite curvature of the tube surface (See Figure 4.2). The formal treatment in the paper by Izumida [9] is to construct an effective Hamiltonian by
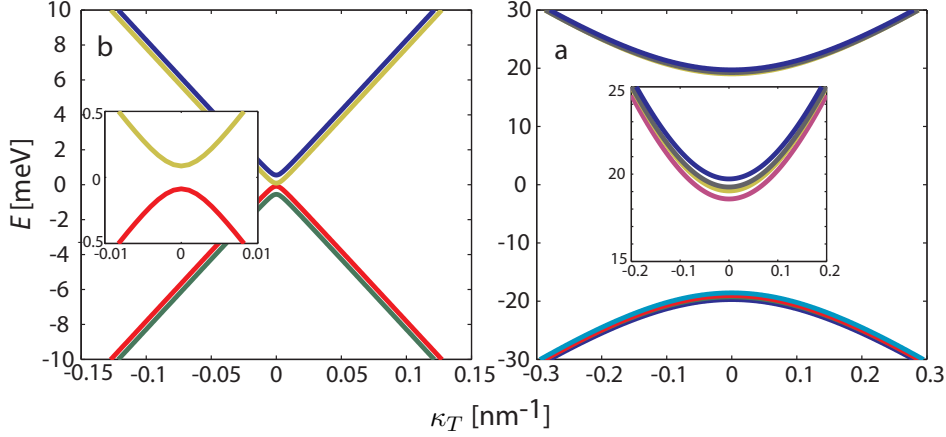
Figure 4.1: Energy dispersion for the lowest lying CNT energy band in the presence of a parallel magnetic field of 4 T. **(a)** (4,4)-armchair tube. The magnetic field induce a bandgap, due to the Aharonov-Bohm effect and splits the energy of the different spin directions due to the Zeeman term. The inset shows a magnified view of the band gap. **(b)** (4,2)-chiral tube. A splitting of the spins also occurs. In addition, since $\mu = -1$ a degeneracy breaking of the **K** and **K**$'$ is seen. The inset shows a magnified view of the conduction band, showing four non-degenerate bands [6].

calculating these effects using a second-order perturbation framework including only nearest-neighbor interactions. An in depth discussion of the procedure is beyond the scope of this thesis. However, a qualitative outline of the calculation scheme will now be given.

The perturbative Hamiltonian consist of two terms $\mathcal{H}' = \alpha\mathcal{H}_{\text{SO}} + \beta\mathcal{H}_{\text{curv}}$, such that the second-order energy correction to the state $|\psi_0\rangle$ becomes [16, p. 256]

$$E_0^2 = \sum_n \frac{\langle\psi_0|\alpha\mathcal{H}_{\text{SO}} + \beta\mathcal{H}_{\text{curv}}|n\rangle\langle n|\alpha\mathcal{H}_{\text{SO}} + \beta\mathcal{H}_{\text{curv}}|\psi_0\rangle}{E_0 - E_n^0}. \tag{4.10}$$

We will thus see contributions from "$\mathcal{H}_{\text{SO}}\mathcal{H}_{\text{SO}}$", "$\mathcal{H}_{\text{curv}}\mathcal{H}_{\text{curv}}$" and the cross terms containing "$\mathcal{H}_{\text{SO}}\mathcal{H}_{\text{curv}}$". The spin-orbit term can for all practical purposes be shown to yield only intra-atomic hopping between the p_z orbital in the π-band and the p_y orbital in the σ-band. In the Izumida paper it is also shown that second order spin-orbit perturbation is negligible compared to the other relevant energies.

However, with the first-order spin-orbit coupling combined with the effect of curvature, i.e. "$\mathcal{H}_{\text{SO}}\mathcal{H}_{\text{curv}}$"– which induces hopping between the σ-orbitals and π-orbitals on adjacent A and B-atoms – electron hopping between the p_z orbitals on adjacent atoms can occur. This is illustrated in Figure 4.2 **(a)** with Δ_1 denoting the hopping parameter. Since the hopping is from atom A to B (and vice versa) it is off-diagonal in AB-space. In addition, because we need to take into consideration all the intermediate $|n\rangle$ states, which are Bloch states that are spread out over the entire tube, a finite hopping back to the p_z orbitals on the same atom occurs. This is illustrated in Figure 4.2 **(b)**, where the green arrow indicate the spreading. Since the effective hopping is intra-atomic, the Δ_0 is diagonal in AB-space. The second order curvature term can be shown to yield a finite hopping between the A and B atom, characterized by the parameter Δ_{g}.
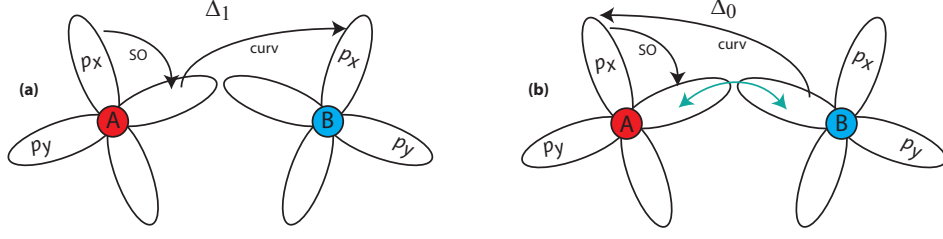
Figure 4.2: Illustration of the possible electron hopping. **(a)** Inter-atomic electron hopping due to spin-orbit coupling and the curvature of the CNT surface. **(b)** On-site spin-orbit hopping, combined with the intermediate states being Bloch states and curvature induced hybridization make hopping back to the beginning p_z orbital possible, yielding diagonal terms in the Hamiltonian in AB-space.

Collecting the above effects, the following effective Hamiltonian is obtained[2]

$$\mathcal{H}_1 = \Delta_0 \tau_3 \sigma_0 S_3 + \Delta_1 \tau_3 \sigma_1 S_3 + \Delta_{\mathrm{g}} \tau_0 \sigma_1 S_0. \tag{4.11}$$

where $\Delta_1 \propto 1/R$, $\Delta_0 \propto \cos(3\theta)/R$ and $\Delta_{\mathrm{g}} \propto \cos(3\theta)/R^2$, where R is the radius from eq. (3.6) and θ is the chiral angle defined in eq. (3.7). For a zig-zag tube of radius 1 nm we get $\Delta_0 = -135\,\mu\mathrm{eV}$, $\Delta_1 = 145\,\mu\mathrm{eV}$ and $\Delta_{\mathrm{g}} = -7$ meV [9]. However, it should be noted that the values are only approximate.

The Δ_{g}-term is off-diagonal in AB-space but diagonal in spin and valley space and corresponds to a change of the circumferential wavevector resulting in bandgaps, even for metallic tubes. For armchair tubes, however, this effect is not present since $\theta = 30^{\mathrm{o}}$. The Δ_1-term splits the energy of opposite spins due to the S_3. The τ_3 inverts the effect for $\mathbf{K}$ and $\mathbf{K}'$ such that the spin up states in $\mathbf{K}$ are energetically degenerate with the spin down states in $\mathbf{K}'$, resulting in two so called Kramer doublets consisting of $\mathbf{K}(\mathbf{K}') \downarrow (\uparrow)$ and $\mathbf{K}(\mathbf{K}') \uparrow (\downarrow)$, respectively, for both the electron and hole band. Time reversal symmetry is thus retained. Experimental evidence of the splitting into Kramer doublets due to the spin-orbit coupling is available [5]. Additionally, the Δ_0-term leads to an asymmetric splitting between the Kramer doublets in the electron and hole band.

In Figure 4.3 the perturbative effects are illustrated for a metallic zig-zag tube of radius 1 nm. In **(a)** $\Delta_0 = 0$ and in **(b)** $\Delta_0 = -135\ \mu\mathrm{eV}$, leading to a decrease in the energy splitting of the conduction bands and an increase in the splitting of the valence bands. In both cases $\Delta_{\mathrm{g}} = -7$meV and $\Delta_1 = 145$meV.

4.3   KK'-mixing

So far all perturbations have been diagonal in valley-space, meaning that no mixing between $\mathbf{K}$ and $\mathbf{K}'$ occurs. States belonging to different valleys can thus be distinguished. However, due to the contacts – which are connected to the tube in order to perform measurements, and the substrate upon which the tube is grown or anything else that breaks rotational symmetry – a finite mixing of the $\mathbf{KK}'$ states needs to be taken into account. This leads to an additional term in the Hamiltonian:

$$\mathcal{H}_{KK'} = \Delta_{KK'} \tau_1 \sigma_0 S_0. \tag{4.12}$$

---

[2]An additional term appearing in $\mathcal{H}_2$ has been neglected, since it corresponds to a change in the translational wavevector, which can be absorbed as a phase constant.
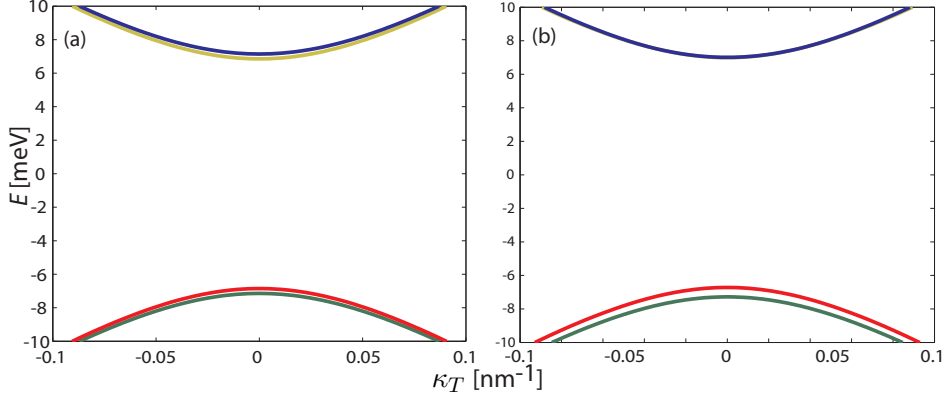
Figure 4.3: Effect of curvature and spin-orbit induced perturbations. **(a)** Energy dispersion with $\Delta_0 = 0$. The splitting of the different spins occurs because of the Δ_1 and is symmetric for the valence and conduction band. **(b)** The splitting becomes asymmetric for the valence and conduction band due to the finite Δ_0 term (-135 μeV).

The mixing can be thought of as electrons orbiting the tube in opposite directions can no longer be distinguished, since $\mathbf{K}(\mathbf{K}')$ corresponds to clockwise (counterclockwise) motion around the nanotube circumference [17]. A realistic value of the mixing parameter is $\Delta_{KK'} = 25\,\mu$eV [1].

4.4   Effective Hamiltonian

When restricting our attention to the lowest lying energy band, i.e. setting $m = 0$, all the perturbative terms can be collected along with the unperturbed one to form a total effective Hamiltonian[3]

$$\mathcal{H} = \hbar v_F(k_g \sigma_1 S_0 + \kappa_T \tau_0 \sigma_2 S_0) + \Delta_{KK'}\tau_1 \sigma_0 S_0 + \Delta_1 \tau_3 \sigma_1 S_3 + \Delta_0 \tau_3 \sigma_0 S_3 + \mu_B \tau_0 \sigma_0 S_3 B, \quad (4.13)$$

where $k_{\mathrm{g}} = \frac{\Phi}{\Phi_0 R}\tau_3 - \frac{\mu}{3R}\tau_0 + \frac{\Delta_{\mathrm{g}}}{v_F}\tau_0$. The combined effect of the perturbations is thus a lifting of the degeneracy of potentially all the energy bands with the corresponding eigenvectors written as linear combinations of all the eight basis vectors from eq. (3.22).

5   Bent Nanotubes

It is natural to ask what happens when the nanotube is not straight. In this case translational invariance can no longer be assumed. However, assuming moderate bending, i.e. the bend radius is taken to be much larger than the inter atomic distances, the tube can locally be considered straight. In the local coordinate system the effective Hamiltonian eq. 4.13 given

---

[3]Choosing a different set of graphene lattice vectors leads to a different $\mathcal{H}_0$. E.g. setting $\mathbf{a}_1 = a(1,0)$ and $\mathbf{a}_2 = a(1/2, \sqrt{(3)}/2)$ we get $\mathcal{H}_0 = \hbar v_F(\kappa_C \tau_3 \sigma_1 S_0 + \kappa_T \tau_0 \sigma_2 S_0)$ which is used in much of the literature and will therefore be adopted as the unperturbed Hamiltonian. The reason for not choosing this set of vectors to begin with is that they lack the beautiful symmetry of those in eq. (3.1).

above generalizes to the following expression, when making the change $\frac{\mathbf{T}}{|\mathbf{T}|} \to \hat{y}'$

$$\mathcal{H} = \hbar v_F[\tau_3\sigma_1 S_0 k_\Phi \mathbf{B} \cdot \hat{y}' - \frac{\mu}{3R}\tau_0\sigma_1 S_0 - i\tau_0\sigma_2 S_0\partial_{y'}] + \Delta_{\mathrm{g}}\tau_0\sigma_1 S_0 + \Delta_{KK'}\tau_1\sigma_0 S_0$$

$$+ \Delta_0\tau_3\sigma_0(\mathbf{S}\cdot\hat{y}') + \Delta_1\tau_3\sigma_1(\mathbf{S}\cdot\hat{y}') + \frac{1}{2}g_s\mu_B[\tau_0\sigma_0(\mathbf{B}\cdot\mathbf{S})], \tag{5.1}$$

where $k_\Phi = \pi R/\Phi_0$, and $\hat{y}'$ is the unit translational vector pointing in the axial direction of the locally straight nanotube segment, such that the momentum operator in this direction reads $p_{y'} = -i\hbar\partial_{y'}$. The local (primed) unit vectors are related to the global ones through the relation (See Figure 5.1)[4]

$$\hat{y}' = \cos\varphi'\hat{y} + \sin\varphi'\hat{x} \tag{5.2}$$
$$\hat{x}' = -\sin\varphi'\hat{y} + \cos\varphi'\hat{x}, \tag{5.3}$$

where $\hat{x}$ and $\hat{y}$ are defined as the unit vectors perpendicular and along the tube axis in the far left side of the tube, which is considered to be semi-infinitely long and straight. In this thesis, only in-tube-plane magnetic fields are considered. With the external magnetic field thus defined in the global basis,

$$\mathbf{B} = B(\cos\varphi\hat{y} + \sin\varphi\hat{x}), \tag{5.4}$$

the last term of the Hamiltonian may be projected onto the local translation and perpendicular vectors $\hat{y}'$ and $\hat{x}'$ in the following way

$$\frac{1}{2}g_s\mu_B\{\tau_0\sigma_0(\mathbf{B}\cdot\mathbf{S})\} = \frac{1}{2}g\mu_B\{\tau_0\sigma_0[B_{||}(\mathbf{S}\cdot\hat{y}') + B_\perp(\mathbf{S}\cdot\hat{x}')]\}, \tag{5.5}$$

where $||$ and $\perp$ denote the components along $\hat{y}'$ and $\hat{x}'$, respectively. By straight-forward geometric considerations, the components $B_{||}$ and $B_\perp$ are found to be

$$B_{||} = B\cos(\varphi - \varphi') \text{ and } B_\perp = B\sin(\varphi - \varphi'). \tag{5.6}$$

5.1   Rotation of spin matrices

The next step is then to project the $\mathbf{S}$ matrix onto the local coordinate axis corresponding to a rotation of the spin operators. For a quantum mechanical system $\mathbf{L} \cdot \hat{n}/\hbar$ is defined as the *generator of rotation* about the direction $\hat{n}$, in the sense that $\exp(i\mathbf{L} \cdot \hat{n}\varphi\hbar)$ corresponds to a rotation through φ around the direction $\hat{n}$ [16, p. 196]. For spin-1/2, which is applicable in our case, the spin-basis transformation from the global to the local coordinate system is thus given

$$\chi' = e^{i(\mathbf{S}\cdot\hat{n})\varphi'/2}\chi, \tag{5.7}$$

where $\hat{n}$ describes an arbitrary direction in the global coordinate system. In Appendix D a thorough analysis of the effect of the rotation is given. When taking the principle quantization direction to be along the tube, i.e. $S_{\hat{y}} \equiv S_3$ and $S_{\hat{x}} \equiv S_1$ the transformation to the local

---

[4]Note that $\hat{x}$ denote the direction perpendicular to the tube, and not $\hat{z}$, which was the case when deriving the expression for the π-band in graphene. This is done in order to be consistent with current notation [1].
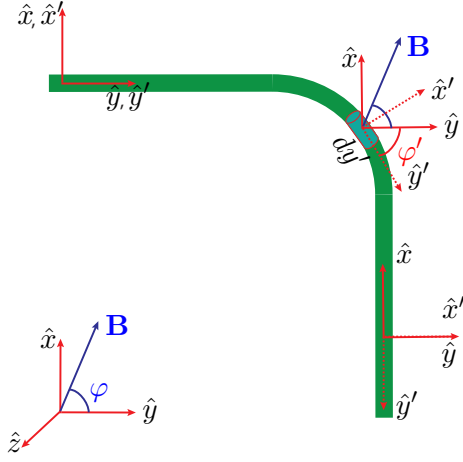
Figure 5.1: Relationship between the global coordinate system y, x (solid red) and the local coordinate system y', x' (dashed red) of a small segment of length dy' (light green) in a bent carbon nanotube (dark green). The external magnetic field, denoted **B** (blue) forms an angle φ with the global translational vector, $\hat{y}$. Both angles are taken to be positive in the counter-clockwise direction.

reference frame corresponds to a rotation about the $\hat{z}$-axis through the angle φ'. The result is

$$\mathbf{S} \cdot \hat{y}' = S_{y'} = \sin(\varphi')S_1 + \cos(\varphi')S_3 \tag{5.8}$$

$$\mathbf{S} \cdot \hat{x}' = S_{x'} = \cos(\varphi')S_1 - \sin(\varphi')S_3, \tag{5.9}$$

such that the local spin-matrices are (not surprisingly) related to the global ones by a unitary rotation matrix.

5.2 Master Hamiltonian

With the given transformation matrices in order, we may rewrite the Hamiltonian eq. (5.1) explicitly in terms of φ and φ' and the global Pauli spin matrices τ_i, σ_i, S_i:

$$\mathcal{H} = \hbar v_F \left\{ \tau_3\sigma_1 S_0 k_\Phi B \cos(\varphi - \varphi') - \frac{\mu}{3R}\tau_0\sigma_1 S_0 - i\tau_0\sigma_2 S_0\partial_{y'} \right\} + \Delta_{\text{g}}\tau_0\sigma_1 S_0 + \Delta_{KK'}\tau_1\sigma_0 S_0$$

$$+ \Delta_1\tau_3\sigma_1 S_{y'} + \Delta_0\tau_3\sigma_0 S_{y'} + \mathscr{B}\tau_0\sigma_0 \left\{ \cos(\varphi - \varphi')S_{y'} + \sin(\varphi - \varphi')S_{x'} \right\} \tag{5.10}$$

where $\mathscr{B} = \frac{1}{2}g_s\mu_B B$. Expanding the expression in all its glory we get the master-Hamiltonian for an arbitrary in-plane magnetic field of the bent carbon nanotube

$$\mathcal{H} = \hbar v_F \left\{ \tau_3\sigma_1 S_0 k_\Phi B \cos(\varphi - \varphi') - i\tau_0\sigma_2 S_0\partial_{y'} \right\} + [\Delta_1\tau_3\sigma_1 + \Delta_0\tau_3\sigma_0] \left[\sin(\varphi')S_1 + \cos(\varphi')S_3 \right]$$

$$+ \mathscr{B}\tau_0\sigma_0 \left\{ \cos(\varphi - \varphi')[\sin(\varphi)S_1 + \cos(\varphi')S_3] + \sin(\varphi - \varphi')[\cos(\varphi')S_1 - \sin(\varphi')S_3] \right\}$$

$$+ \Delta_{\text{g}}\tau_0\sigma_1 S_0 + \Delta_{KK'}\tau_1\sigma_0 S_0. \tag{5.11}$$

In places where translational symmetry can be assumed, i.e. in the infinitely straight part where $\varphi' = 0$, we make the replacement: $-i\partial_{y'} \to \kappa_{y'}$ and recover eq. (4.13).

6 Conductance Through Bent Nanotubes

The results derived so far are based on theoretical models, and with the study of bent nanotubes being fairly new, it would be interesting to relate the models to something measurable. An obvious starting point is to measure the conductance through a bent tube and evaluate the influence of the bending. In making theoretical predictions for the conductance, the first step is to obtain the transmission coefficient. This is the topic of the present section.

6.1 Derivation of the scattering matrix

As in most of quantum mechanics, the starting point of this derivation is the time-independent Schrödinger equation. Applying the Hamiltonian eq. (5.11) to $|\Psi(y')\rangle$ – which is the eight-dimensional wavevector for electrons in the tube written in the basis $\{|\tau, \sigma, S\rangle\}$ from eq. (3.22) – we get

$$\mathcal{H}|\Psi(y')\rangle = E|\Psi(y')\rangle. \tag{6.1}$$

Examining the Hamiltonian in eq. (5.11) we find that it has the form

$$\mathcal{H} = i\partial_{y'}\mathbf{M}_0 + \mathbf{M}_1(\varphi, \varphi'),$$

i.e. there is a part which is constant, $\mathbf{M}_0$, and one which depends on the position along the tube axis through the angle between the tube and the applied magnetic field, $\mathbf{M}_1(\varphi, \varphi')$. The matrices are defined:

$$\mathbf{M}_0 \equiv -\hbar v_F \tau_o \sigma_2 S_0 \tag{6.2}$$

and

$$\begin{aligned}
\mathbf{M}_1(\varphi, \varphi') \equiv {}& \hbar v_F \left\{\tau_3\sigma_1 S_0 \left[k_c + k_\Phi B \cos(\theta)\right]\right\} + \left[\tau_3\sigma_1\Delta_1 + \tau_3\sigma_0\Delta_0\right]\left[\sin(\varphi')S_1 + \cos(\varphi')S_3\right] \\
& + \mathscr{B}\tau_0\sigma_0 g \left\{\cos(\theta)[\sin(\varphi')S_1 + \cos(\varphi')S_3] + \sin(\theta)[\cos(\varphi')S_1 - \sin(\varphi')S_3]\right\} \\
& + \tau_1\sigma_0 S_0\Delta_{KK'}.
\end{aligned} \tag{6.3}$$

The Schrödinger equation (6.1) can thus be recast in the following way

$$\left[i\partial_{y'}\mathbf{M}_0 + \mathbf{M}_1(\varphi, \varphi')\right]|\Psi(y')\rangle = E|\Psi(y')\rangle. \tag{6.4}$$

6.1.1 Wavefunction integration

Rearrangement of eq. (6.4) yields the set of first-order differential equations

$$\boxed{\frac{\partial}{\partial y'}|\Psi(y')\rangle = i\mathbf{M}_0^{-1}\left(\mathbf{M}_1(\varphi, \varphi') - E\right)|\Psi(y')\rangle.} \tag{6.5}$$

With the wavefunction at the starting point of the bent ($y' = 0$) described by $|\Psi_0\rangle$ as a boundary condition, the set has the solution

$$|\Psi(y')\rangle = \exp\left[iy'\mathbf{M}_0^{-1}(\mathbf{M}_1(\varphi, \varphi') - E)\right]|\Psi_0\rangle, \tag{6.6}$$

since it fits the boundary conditions and fulfills eq. (6.5). So far everything is exact. When performing numerical calculations, we assume the tube is straight in a small segment of length dy' (Figure 5.1), such that $\mathbf{M}_1$ locally remains constant and the solution is valid.

We denote the argument $\mathbf{M}_0^{-1}(\mathbf{M}_1(\phi, \varphi') - E)$ by $\mathbf{A}$. In Appendix E it is shown that the exponential term in eq. (6.6) can be written $\mathbf{U}\mathcal{D}\mathbf{U}^{-1}$, where

$$\mathcal{D} = \begin{pmatrix} e^{iy'\lambda_1} & 0 & \cdots \\ 0 & \ddots & \vdots \\ \vdots & \cdots & e^{iy'\lambda_8} \end{pmatrix}, \tag{6.7}$$

with λ_i denoting the eigenfunctions of $\mathbf{A}$ and $\mathbf{U}$ is the matrix consisting of the eigenvectors of $\mathbf{A}$. The wavefunction thus becomes

$$|\Psi(y')\rangle = \mathbf{U}\mathcal{D}\mathbf{U}^{-1}|\Psi_0\rangle. \tag{6.8}$$

Dividing the tube into N locally straight segments, each of length dy', an expression for the wavefunction at $y' = N dy'$, corresponding to the far right side of the tube, is established

$$|\Psi_N\rangle \equiv |\Psi(N dy')\rangle = \mathbf{U}_N \mathcal{D}_N \mathbf{U}_N^{-1} \cdots \mathbf{U}_2 \mathcal{D}_2 \mathbf{U}_2^{-1} \mathbf{U}_1 \mathcal{D}_1 \mathbf{U}_1^{-1}|\Psi_0\rangle \equiv \mathcal{M}|\Psi_0\rangle, \tag{6.9}$$

where the subscript denote the segment number in which the eigenvalues and eigenfunctions are found.

6.1.2 Determining the wavefunction in the straight tube

In order to perform the stepwise integration of eq. (6.5) along the nanotube, we thus need the total wavefunction in the straight part of the tube where translational invariance is assumed, $|\Psi_L(y')\rangle$. It may be expressed as a linear combination of the right and left going eigenstates of the Hamiltonian in the straight tube, which are found in the four partially filled conduction bands[5]. We neglect the eigenfunctions in the fully filled valence bands, since they do not contribute to electronic transport.

The process of determining the correct eigenfunctions amounts to choosing the κ_y's such that the energies of the 8 eigenstates (four left traveling and four right traveling) in the conduction bands match the given Fermi energy E. The precise location of the Fermi energy is determined partially by the CNT itself and partially by the substrate upon which the tube is situated, arising from a higher or lower degree of electronic doping. In addition, one or more back-gates may be included to electrostatically alter the Fermi energy. In the case when the matching with a real κ_y is not possible, because the band in question lies above the Fermi energy such that $\kappa_y \in \mathbb{C}$, it is an evanescent wave, which in the semi-infinite tube completely dies out. In Figure 6.1 two different Fermi-energies are illustrated; one for which all the $\kappa_{y'}$s are real (E_2) and one for which two are imaginary and two are real (E_1).

The 8 normalized eigenfunctions of the Hamiltonian are themselves linear combinations of the $\{|\tau, \sigma, S\rangle\}$-basis given in eq. (3.22). We denote them by $\boldsymbol{\mu}_{ja}(\kappa_{ja})$ and $\boldsymbol{\mu}_{jb}(\kappa_{jb})$ where a corresponds to right-movers and b corresponds to left-movers. j denote which of the four conduction bands the state belongs to. E.g. in Figure 6.1 $\boldsymbol{\mu}_{1a}$ is the right traveling state in the first band that matches E_1 for κ_{y1a}. We denote the weights of the j'th right(left) traveling state by the column vectors $\mathbf{W}_a(\mathbf{W}_b)$, where

$$\mathbf{W}_b = \begin{pmatrix} w_{1a} \\ w_{2a} \\ w_{3a} \\ w_{4a} \end{pmatrix}, \ \mathbf{W}_b = \begin{pmatrix} w_{1b} \\ w_{2b} \\ w_{3b} \\ w_{4b} \end{pmatrix}. \tag{6.10}$$

E.g. w_{1a} is the weight of the right-traveling eigenstate in the first band in the total wavefunction. The total wavefunction, which is a sum of left and right movers, can thus be written

$$|\Psi_L(y')\rangle = \underbrace{\begin{bmatrix} \boldsymbol{\mu}_{1a} & \boldsymbol{\mu}_{2a} & \boldsymbol{\mu}_{3a} & \boldsymbol{\mu}_{4a} \end{bmatrix}}_{\bar{\bar{\boldsymbol{\mu}}}_a} \mathcal{K}_a \mathbf{W}_a + \underbrace{\begin{bmatrix} \boldsymbol{\mu}_{1b} & \boldsymbol{\mu}_{2b} & \boldsymbol{\mu}_{3b} & \boldsymbol{\mu}_{4b} \end{bmatrix}}_{\bar{\bar{\boldsymbol{\mu}}}_b} \mathcal{K}_b \mathbf{W}_b. \tag{6.11}$$

---

[5]The velocity of a wave packet is determined as the gradient of the energy dispersion, such that waves traveling to the left (right) is associated with a negative (positive) slope of the dispersion relation with respect to κ_y.
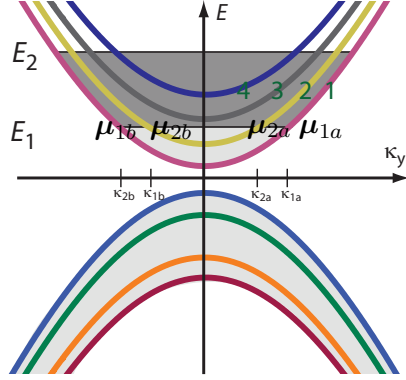
Figure 6.1: Energy dispersion including nanotube perturbation. Two different Fermi-levels, E_1 and E_2 are illustrated. Grey indicate occupied states. For E_1 the corresponding κ_y values are real for the two lowest lying conduction bands while they are imaginary for the next two, since they are above the Fermi energy. For E_2 all the κ_y-values are real.

$\bar{\bar{\boldsymbol{\mu}}}_{a(b)}$ is thus the matrix constructed from the four eigenfunctions belonging to the j'th band of right(left)-traveling waves. The $\mathcal{K}_a$ and $\mathcal{K}_b$ tack on the plane-wave Bloch factor on the j'th eigenfunction, i.e.

$$\mathcal{K}_\alpha = \begin{pmatrix} e^{\kappa_{1\alpha}y'} & 0 & 0 & 0 \\ 0 & e^{i\kappa_{2\alpha}y'} & 0 & 0 \\ 0 & 0 & e^{i\kappa_{3\alpha}y'} & 0 \\ 0 & 0 & 0 & e^{i\kappa_{4\alpha}y'} \end{pmatrix}. \tag{6.12}$$

where $\alpha = a(b)$ for right(left)-traveling waves.

On the other side of the bend the tube is again assumed to be semi-infinitely long and straight. The total wavefunction, $|\Psi_R(y'')\rangle$, is again constructed as a linear combination of eigenstates of the Hamiltonian in the form of right and left going plane-waves, expressed by the weights $\mathbf{W}_c$ and $\mathbf{W}_d$, respectively. However, the Hamiltonian is not necessarily the same as in the beginning.[6] Nevertheless, the process of finding the allowed states and matching corresponding κ_y's to the constant energy is completely analogous to the one described above. The total wavefunction is thus written

$$|\Psi_R(y'')\rangle = \underbrace{\begin{bmatrix} \boldsymbol{\mu}_{1c} & \boldsymbol{\mu}_{2c} & \boldsymbol{\mu}_{3c} & \boldsymbol{\mu}_{4c} \end{bmatrix}}_{\bar{\bar{\boldsymbol{\mu}}}_c}\mathcal{K}_c\mathbf{W}_c + \underbrace{\begin{bmatrix} \boldsymbol{\mu}_{1d} & \boldsymbol{\mu}_{2d} & \boldsymbol{\mu}_{3d} & \boldsymbol{\mu}_{4d} \end{bmatrix}}_{\bar{\bar{\boldsymbol{\mu}}}_d}\mathcal{K}_d\mathbf{W}_d. \tag{6.13}$$

The $\mathcal{K}_\beta$'s, $\beta \in \{c, d\}$ once again tack on the Bloch factor, now written in a different reference frame y'', such that

$$\mathcal{K}_\beta = \begin{pmatrix} e^{i\kappa_{1\beta}y''} & 0 & 0 & 0 \\ 0 & e^{i\kappa_{2\beta}y''} & 0 & 0 \\ 0 & 0 & e^{i\kappa_{3\beta}y''} & 0 \\ 0 & 0 & 0 & e^{i\kappa_{4\beta}y''} \end{pmatrix}, \tag{6.14}$$

where $\beta = c(d)$ for right(left)-traveling waves. In Figure 6.2 **(a)** a schematic overview of the incoming and outgoing waves is given. **a** denote the incoming, right-traveling waves from the left and **b** signify left-traveling reflected waves. **c** indicate the transmitted, right-traveling waves while **d** are left-traveling incoming waves from the right.

---

[6]This depends on the final orientations of the tube. If it returns to the same configurations, in the sense that the orientations of the tube with respect to the applied magnetic field is equivalent to the beginning part, the Hamiltonian – and as a result the eigenfunctions – will be the same.
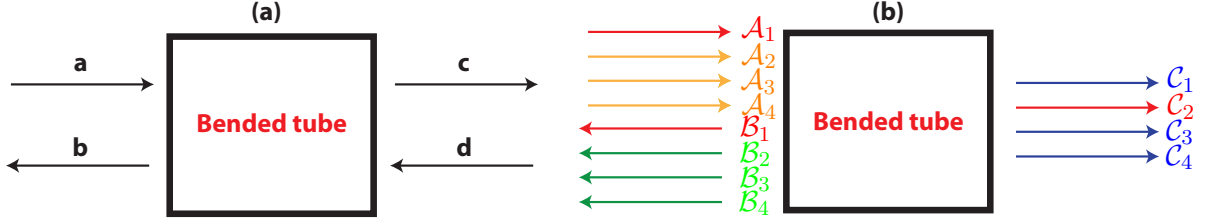
Figure 6.2: Schematic overview of the incoming and outgoing waves. **(a)** General case, where **a** and **c** are the right-going incoming and transmitted waves, respectively. **b** denote the reflected waves while **d** indicate the incoming waves from the right. **(b)** Example where channels $\mathcal{A}_1, \mathcal{B}_1$ and $\mathcal{C}_2$ are closed. See section 6.1.3 for details. Orange arrows indicate open incoming channels, green indicate open reflected channels while the blue arrows correspond to open transmissive. Red indicate closed channels.

6.1.3   Wavefunction matching

We now assume that there are no incoming waves from the right, which corresponds to $\mathbf{W}_d = 0$. Setting $y' = 0$ at the beginning of the bent, such that $|\Psi_L(y' = 0)\rangle \equiv |\Psi_0\rangle$ yields $\mathcal{K}_a = \mathcal{K}_b = \mathbf{1}$. Absorbing the remaining Bloch factors into the weight coefficients in $\mathbf{W}_c$ we may set $|\Psi_R\rangle_{y'=Ndy'} \equiv |\Psi_N\rangle$. Performing the discretization from eq. (6.9) we thus get an equation which relates the eigenstates and weight vectors on the left and right side of the bend

$$\bar{\boldsymbol{\mu}}_c \mathbf{W}_c = \mathcal{M}\left[\bar{\boldsymbol{\mu}}_a \mathbf{W}_a - \bar{\boldsymbol{\mu}}_b \mathbf{W}_b\right]. \tag{6.15}$$

which can be rearranged such that

$$\bar{\bar{\boldsymbol{\mu}}}_c \mathbf{W}_c - \mathcal{M}\bar{\bar{\boldsymbol{\mu}}}_b \mathbf{W}_b = \mathcal{M}\bar{\bar{\boldsymbol{\mu}}}_a \mathbf{W}_a. \tag{6.16}$$

We now look separately at the contributions from the four channels of incoming waves: $\mathcal{A}_1, \mathcal{A}_2, \mathcal{A}_3$ and $\mathcal{A}_4$, which correspond to the right-traveling states in band 1 to 4, respectively. We define the j'th weight vectors for the transmitted and reflected waves corresponding to the $\mathcal{A}'_j$th channel by

$$\mathbf{W}_{jc} = \begin{pmatrix} w_{1jc} \\ w_{2jc} \\ w_{3jc} \\ w_{4jc} \end{pmatrix}, \quad \mathbf{W}_{jb} = \begin{pmatrix} w_{1jb} \\ w_{2jb} \\ w_{3jb} \\ w_{4jb} \end{pmatrix}. \tag{6.17}$$

The row numbers indicate the weight in the total wavefunction of the transmitted and reflected eigenstate of the corresponding channels (bands), which we denote $\mathcal{C}_1, \mathcal{C}_2, \mathcal{C}_3$ and $\mathcal{C}_4$ for the transmissive channels (bands) and $\mathcal{B}_1, \mathcal{B}_2, \mathcal{B}_3$ and $\mathcal{B}_4$ for the reflective channels (bands). E.g. w_{11c} is the weight of $\boldsymbol{\mu}_{1c}$ in the wavefunction in eq. (6.13) when regarding contributions from incoming waves in channel 1 i.e., $\mathcal{A}_1$.

Since evanescent states die out in the infinite straight tube, we neglect them in the total wavefunctions. An evanescent state in the j'th band (on either side of the tube) will thus correspond to the j'th channel being closed. Hence, $\mathcal{A}_j, \mathcal{B}_j$ or $\mathcal{C}_j$ all have the possibility of being closed. Whether this is the case depends on the location of the j'th band compared to the given Fermi energy. However, since the dispersion relation is symmetric around $\kappa_y = 0$; if state $\boldsymbol{\mu}_{ja}$ is evanescent, so is $\boldsymbol{\mu}_{jb}$ and $\mathcal{A}_j$ and $\mathcal{B}_j$ are both closed. Whenever a channel is closed, the corresponding eigenfunctions and weight indices need to be discarded. To perform

this deed, we define the operators Λ_{eig} and Λ_{coeff}. Λ_{eig} operates in the way that whenever a channel is closed, it removes the corresponding eigenfunction. Λ_{coeff} operates in an equivalent way, however it discards the weight coefficients of the closed channels. With this notation eq. (6.16) may be written in the following form, where we take into account the contributions from all channels at once:

$$\begin{bmatrix} \bar{\bar{\boldsymbol{\mu}}}_c \Lambda_{\text{eig}} & -\mathcal{M} \bar{\bar{\boldsymbol{\mu}}}_b \Lambda_{\text{eig}} \end{bmatrix} \begin{pmatrix} \mathbf{W}_{1c} & \mathbf{W}_{2c} & \mathbf{W}_{3c} & \mathbf{W}_{4c} \\ \mathbf{W}_{1b} & \mathbf{W}_{2b} & \mathbf{W}_{3b} & \mathbf{W}_{4b} \end{pmatrix} \Lambda_{\text{coeff}} = \mathcal{M} \bar{\bar{\boldsymbol{\mu}}}_a \Lambda_{\text{eig}}. \tag{6.18}$$

The 2×4 matrix is denoted the *coefficient matrix*, which is an 8×4 matrix when all the coefficients are written out. The columns correspond to the incoming channels, $\mathcal{A}_1 - \mathcal{A}_4$, row 1-4 denote the transmissive channels $\mathcal{C}_1 - \mathcal{C}_4$ while row 4-8 denote the reflective channels $\mathcal{B}_1 - \mathcal{B}_4$. For clarity we provide an example of how the operators Λ_{coeff} and Λ_{eig} work. E.g. say $\boldsymbol{\mu}_{1a}$ is an evanescent state, such that channel $\mathcal{A}_1$ is closed, so will $\mathcal{B}_1$ due to symmetry. If we also assume $\boldsymbol{\mu}_{2c}$ is an evanescent state, channel $\mathcal{C}_2$ will be closed. In this case the action of Λ_{coeff} is to reduce the coefficient matrix in the following way

$$\begin{array}{c} \\ \mathcal{C}_1 \\ \mathcal{C}_2 \\ \mathcal{C}_3 \\ \mathcal{C}_4 \\ \mathcal{B}_1 \\ \mathcal{B}_2 \\ \mathcal{B}_3 \\ \mathcal{B}_4 \end{array} \begin{array}{cccc} \mathcal{A}_1 & \mathcal{A}_2 & \mathcal{A}_3 & \mathcal{A}_4 \\ \begin{pmatrix} w_{11c} & w_{21c} & w_{31c} & w_{41c} \\ w_{12c} & w_{22c} & w_{32c} & w_{42c} \\ w_{13c} & w_{23c} & w_{33c} & w_{43c} \\ w_{14c} & w_{24c} & w_{34c} & w_{44c} \\ w_{11b} & w_{21b} & w_{31b} & w_{41b} \\ w_{12b} & w_{22b} & w_{32b} & w_{42b} \\ w_{13b} & w_{23b} & w_{33b} & w_{43b} \\ w_{14b} & w_{24b} & w_{34b} & w_{44b} \end{pmatrix} \end{array} \xrightarrow{\Lambda_{\text{coeff}}} \begin{array}{c} \\ \mathcal{C}_1 \\ \mathcal{C}_3 \\ \mathcal{C}_4 \\ \mathcal{B}_2 \\ \mathcal{B}_3 \\ \mathcal{B}_4 \end{array} \begin{array}{ccc} \mathcal{A}_2 & \mathcal{A}_3 & \mathcal{A}_4 \\ \begin{pmatrix} w_{11c} & w_{11c} & w_{11c} \\ w_{23c} & w_{33c} & w_{43c} \\ w_{24c} & w_{34c} & w_{44c} \\ w_{22b} & w_{32b} & w_{42b} \\ w_{23b} & w_{33b} & w_{43b} \\ w_{24b} & w_{34b} & w_{44b} \end{pmatrix} \end{array}. \tag{6.19}$$

Correspondingly, the number of eigenstates are reduced by the operator Λ_{eig}. For the given example the reduction is done as follows

$$\begin{bmatrix} \boldsymbol{\mu}_{1a} & \boldsymbol{\mu}_{2a} & \boldsymbol{\mu}_{3a} & \boldsymbol{\mu}_{4a} \\ \boldsymbol{\mu}_{1b} & \boldsymbol{\mu}_{2b} & \boldsymbol{\mu}_{3b} & \boldsymbol{\mu}_{4b} \\ \boldsymbol{\mu}_{1c} & \boldsymbol{\mu}_{2c} & \boldsymbol{\mu}_{3c} & \boldsymbol{\mu}_{4c} \end{bmatrix} \xrightarrow{\Lambda_{\text{eig}}} \begin{bmatrix} \boldsymbol{\mu}_{2a} & \boldsymbol{\mu}_{3a} & \boldsymbol{\mu}_{4a} \\ \boldsymbol{\mu}_{2b} & \boldsymbol{\mu}_{3b} & \boldsymbol{\mu}_{4b} \\ \boldsymbol{\mu}_{1c} & \boldsymbol{\mu}_{3c} & \boldsymbol{\mu}_{4c} \end{bmatrix} \tag{6.20}$$

The example is illustrated in Figure 6.2 **(b)**. Rearranging eq. (6.18), a final expression for the coefficient matrix in terms of the $\mathcal{M}$ matrix and the eigenfunctions in the beginning and end of the tube is established:[7]

$$\begin{pmatrix} \mathbf{W}_{1c} & \mathbf{W}_{2c} & \mathbf{W}_{3c} & \mathbf{W}_{4c} \\ \mathbf{W}_{1b} & \mathbf{W}_{2b} & \mathbf{W}_{3b} & \mathbf{W}_{4b} \end{pmatrix} \Lambda_{\text{coeff}} = \begin{bmatrix} \bar{\bar{\boldsymbol{\mu}}}_c \Lambda_{\text{eig}} - \mathcal{M} \bar{\bar{\boldsymbol{\mu}}}_b \Lambda_{\text{eig}} \end{bmatrix}^{-1} \mathcal{M} \bar{\bar{\boldsymbol{\mu}}}_a \Lambda_{\text{eig}} = \mathcal{S}, \tag{6.21}$$

where $\mathcal{S}$ is the *scattering matrix*. For the scattering matrix we define

$$\mathcal{S} \equiv \begin{pmatrix} \mathbf{t} \\ \mathbf{r} \end{pmatrix} \tag{6.22}$$

such that the *transmission* and *reflection matrix* $\mathbf{t}$ and $\mathbf{r}$, respectively, corresponds to

$$\mathbf{t} = \begin{pmatrix} \mathbf{W}_{1c} & \mathbf{W}_{2c} & \mathbf{W}_{3c} & \mathbf{W}_{4c} \end{pmatrix} \Lambda_{\text{coeff}} \text{ and } \mathbf{r} = \begin{pmatrix} \mathbf{W}_{1b} & \mathbf{W}_{2b} & \mathbf{W}_{3b} & \mathbf{W}_{4b} \end{pmatrix} \Lambda_{\text{coeff}}. \tag{6.23}$$

---

[7]If the dimensions have been reduced, the matrix $\begin{bmatrix} \bar{\bar{\boldsymbol{\mu}}}_c \Lambda_{\text{eig}} & -\mathcal{M} \bar{\bar{\boldsymbol{\mu}}}_b \Lambda_{\text{eig}} \end{bmatrix}$ is not necessarily square, and the inversion is done as a pseudo inverse through the Moore-Penrose method in which $\mathbf{A}^{-1} = (\mathbf{A}^\dagger \mathbf{A})^{-1} \mathbf{A}^\dagger$.

Since the transmission is given as the sum of all the $|w_{ijc}|^2$ terms, corresponding to the contributions from all available transmissive channels, it becomes

$$T = \sum_{i=1}^{N_T} \sum_{j=1}^{N_I} |\mathbf{t}(ij)|^2 = \mathrm{Tr}(\mathbf{t}^\dagger \mathbf{t}), \tag{6.24}$$

and the reflection, which is the sum of all the $|w_{ijb}|^2$ terms, is written

$$R = \sum_{i=1}^{N_R} \sum_{j=1}^{N_I} |\mathbf{r}(ij)|^2 = \mathrm{Tr}(\mathbf{r}^\dagger \mathbf{r}), \tag{6.25}$$

where $N_T(N_I/N_R)$ is the number of open transmissive (incoming/reflective) channels; $N_i = N_T$ due to symmetry. The sum of the reflection and transmission has to equal the total number of open incoming channels, since the flux has to be preserved. Hence the scattering matrix $\mathcal{S}$ has to obey

$$T + R = \mathrm{Tr}(\mathbf{t}^\dagger \mathbf{t}) + \mathrm{Tr}(\mathbf{r}^\dagger \mathbf{r}) = \mathrm{Tr}(\mathcal{S}^\dagger \mathcal{S}) = N_I. \tag{6.26}$$

6.2 From transmission to conductance

When having obtained the transmission for the bent carbon nanotube the next step is to relate it to a measurable quantity, namely the conductance. It can be shown that for a 1-D system with N non-degenerate channels the current, when assuming perfect transmission, is given

$$I = N \frac{e^2}{h} V, \tag{6.27}$$

where e^2/h is the conductance quantum ϕ_0 [13, p. 143] and V is determined as the difference in chemical potential between the left and right electrodes. In the case where transmission is not perfect we still get a simple expression for the conductance. When assuming zero temperature we get

$$G = \frac{e^2}{h} T. \tag{6.28}$$

This is the famous *Landauer Formula* [18], which provides us with the master equation of this thesis

$$\boxed{G = \frac{e^2}{h} \mathrm{Tr}(\mathbf{t}^\dagger \mathbf{t})} \tag{6.29}$$

By tuning the voltage difference and applying a constant magnetic field across the bent nanotube we expect to see a higher or lower degree of conductance depending on the Fermi energy. When sweeping this energy, which is done by applying a back-gate to the sample, we expect to see changes in the conductance along with some (hopefully) exciting features.

Predicting and analyzing these features will be the topic of the remainder of this thesis, in which theoretical conductances of various nanotube configurations and external parameters will be investigated through numerical simulations, using the procedures developed in this section.

7   Simulation of Conductance Through Bent Nanotubes

The integration routine for developing the reflection and transmission and thus the conductance for bent tubes has been implemented using MATLAB. The routine consists mainly of for-loops and eigenvalue and eigenfunction finding. In Appendix F a walk-through of the simulation along with examples from the script is given.

7.1   Methods

Many setups for measuring the conductance of nanotubes are possible. However, in all cases the tube is placed in between one or more electrodes through which current is conducted. In addition, one or more back-gates may interact electrostatically with the tube [19]. In this thesis we consider the four geometries depicted in Figure 7.1. **(a)** a *hill-like* tube, which is characterized by the slope and length of the hill. **(b)** a *staircase-like* tube which is constructed by linking two of the configurations from **(a)** through a straight section, which we set to 50 or 100 nm. **(c)** A *harmonically* shaped tube, described by a cosine function undergoing one oscillation, in which we control the bending through the amplitude and the period. **(d)** A ω shaped tube, which is the same as in **(c)**, but with the cosine function undergoing two oscillations. In all cases the straight sections in the beginning and end of the tubes (indicated in red) are considered to be long enough that evanescent modes can be neglected. For all the configurations the tube orientation with respect to an applied magnetic field is the same in the beginning and end of the tube. The Fermi energy is chosen such that all of the 4 channels are open, i.e. $N_I = N_R = N_T = 4$. In Figure H.1 and H.2 in Appendix H a detailed view of the tube geometries, including the angular dependence on position, is given.

   Prior to simulating the conductance of the bent tubes, the script was run on a straight tube, in which the Fermi energy was varied such that not all of the channels were open. In all the simulations we used a nanotube of radius 2 nm and the perturbation parameters $\Delta_0 = 145 \ \mu$eV, $\Delta_1 = -135 \ \mu$eV, $\Delta_g = -7$ meV and $\Delta_{KK'} = 25 \ \mu$eV as determined in section 4.2[8].

7.2   Results

The results can be found in Appendix G. Figure G.1 shows simulations on a 500 nm straight nanotube for various magnetic field orientations and strengths. In all cases clear step-like behavior in the conductance of integer values of the conductance quantum $\phi_0 = e^2/h$ is visible. In **(e)**, where the magnetic field is turned off, the step is $2\phi_0$. In **(a)** and **(b)**, corresponding to a magnetic field of 2 T with the angle $\varphi = 0$ and $\varphi = 30^\circ$, fluctuations at the transitions $2\phi_0 \rightarrow 3\phi_0$ are seen. In addition, in **(a)** fluctuations also appear at the transition $\phi_0 \rightarrow 2\phi_0$, though they are less pronounced.

Figure G.2 shows the result of the simulations for the hill-like conformation for various tube bendings with a magnetic field of 9 T aligned perpendicular to the tube. In all cases the conductance (transmission) increases with increasing energy. The conductance of the straight tube in **(a)**, which acts as a control, is $4\phi_0$ for all the used energies. Integer steps of ϕ_0 in the

---

[8]Here the calculation was for a 1 nm tube radius. However, it was noted that the parameters are approximate, so we have taken the liberty of applying them to a nanotube of radius 2 nm in order to see an enhanced Aharonov-Bohm effect, which is proportional to the radius.
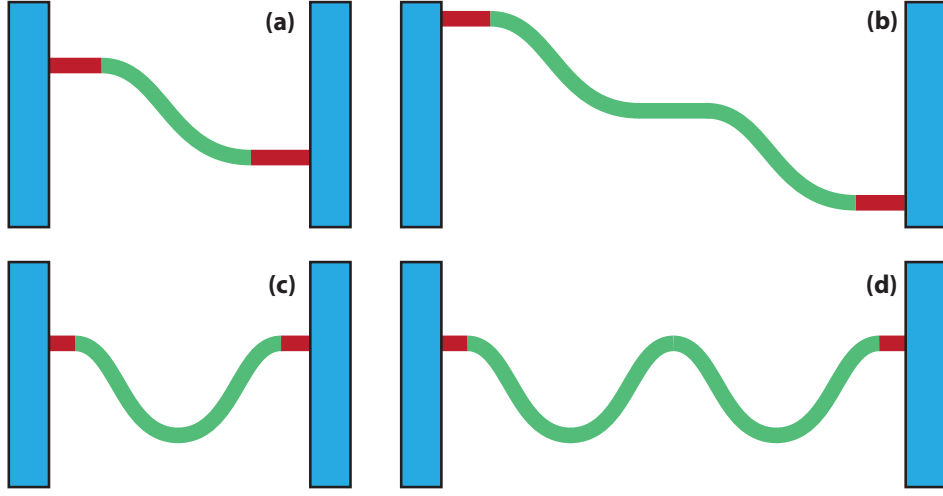
Figure 7.1: Experimental setup for measuring the conductance. **(a)** Two straight sections (red) are connected to the electrodes (blue) with the hill-like shaped tube (green) in between. **(b)** Two of the segments from **(a)** are placed around a straight segment of varying length. **(c)** and **(d)** Same as **(a)** but for a harmonically shaped function undergoing one and two oscillations, respectively.

conductance is visible in **(c)** and **(d)**, where it changes from $3\phi_0$ to $4\phi_0$. **(b)** shows a fractional step of ϕ_0. **(e)** and **(f)** show the results of the simulations for the stairway-like tube, which is constructed by connecting two 100 nm bend hill-like tubes (purple graph in Figure H.1) through a straight segment of 50 and 100 nm, respectively. In **(e)** the conductance shows a steady level of $3\phi_0$ until the energy reaches approximately 8.45 meV, after which the conductance rises to $4\phi_0$. A peak in the conductance (transmission) occurs around 8.35 meV. A corresponding dip in the reflection is visible at the same energy. **(f)** The conductance pattern resembles that of **(e)**, however the position of the peak/dip, which are both increased, is displaced.

Figure G.3 **(a)**-**(d)** show the result of simulations performed on the harmonically shaped tube for various degrees of bending with a magnetic field of 9 T aligned perpendicular to the tube. Again the straight tube yields conductance of $4\phi_0$. The data show a tendency of the sum of the transmission and reflection not being equal to 4 – especially for large bending in the low energy regime, e.g. Figure G.3 **(d)** and Figure G.4 **(b)** and **(d)**. In all the simulations the sum nevertheless converges towards 4 with increasing energy.

In **(c)** and **(d)** a conductance plateau of $3\phi_0$ is visible followed by a gradual increase to a conductance of $4\phi_0$. In both cases the increase occurs over an energy span of approximately 0.1 meV. In **(d)** an additional step is visible, where the conductance increases from approximately $2.2\phi_0$ to $3\phi_0$ over an energy span of 0.2 meV. In **(b)** a fractional step of ϕ_0 occurs.

Additional simulations for the conductance in which the magnetic field is varied are shown in Figure G.3 **(e)** and **(f)**. The tube configuration is the same as in **(d)**, but with the magnetic field turned off and set to 7 T in **(e)** and **(f)**, respectively. In **(e)** a step in the conductance of $2\phi_0$ is visible, but a peak in the sum of the transmission and reflection to around 5.5 occurs at the transition. The behavior of the conductance in **(f)** resembles that of **(d)** just displaced to lower energies; however the first conductance step is missing.

Figure G.4 shows simulations for the ω shaped tube, which is build by placing two 100 nm bending tubes (Figure H.2 purple curve) in tandem. **(a)**, **(b)** and **(c)** corresponds to a magnetic field of 5, 7 and 9 T aligned perpendicular to the tube, respectively. In **(a)** the conductance is close to $4\phi_0$ for all energies. In **(b)** an increase in the conductance from $G \approx 3\phi_0 \rightarrow 4\phi_0$ over an energy range of around 0.2 meV is visible. At an energy of circa 8.05 meV a dip in the conductance (and a peak in the reflection) is seen. At an energy of around 8.2 meV the situation is reversed; here a peak in the conductance and a dip in the reflection is visible. In **(c)** an extra conductance step, $G \approx 2.2\phi_0 \rightarrow 3\phi_0$, is visible at an energy of approximately 8.2 meV. Again, dips and peaks in the conductance and reflections appear. In both **(b)** and **(c)** the sum of the transmission and reflection fails to equal 4 for energies lower that 8.5 meV. However, in all the simulations, the sum converger towards 4 as the energy increases.

7.3 Discussion

Straight-tube. The quantized conductance steps and observed plateaus in Figure G.1 are characteristic for ballistic transport through a 1-D system, and has also been reported in CNTs [4, 19, 20, 21]. However, the experimentally observed steps have been of $2e^2/h$ or $4e^2/h$. Previous theoretical studies also predicted steps of $2e^2/h$ ($4e^2/h$) [22], depending on the presence (absence) of a magnetic field, but here spin-orbit and curvature effects were not taken into consideration.

The behavior of the conductance may be described in a way similar to that of a quantum point contact (QPC). Here a step-like conductance is seen when sweeping a gate voltage, since this brings the allowed states into the window defined by the chemical potentials of the leads [14, p.535]. Whenever a state is in the window, there will be a propagating solution yielding conductance in units of the conductance quantum ϕ_0. In this sense, the process of bringing the states into the window may be thought of as varying a potential barrier which the states have to pass through.

The incoming waves of the bent nanotube are defined by a given Fermi energy. If a given conduction band lies above this energy, the corresponding state in the band is an evanescent mode, which is neglected in the infinite straight tube. In order for it to become a propagating solution, the Fermi energy has to be larger than the band in question, i.e. there is a potential barrier of finite height, but infinite width (in the straight tube) that the waves need to overcome. In Figure 7.2 **(a)** and **(b)** the conduction bands for a magnetic field at $\varphi = 30^{\text{o}}$ and $\varphi = 60^{\text{o}}$, corresponding to Figure G.1 **(b)** and **(c)**, respectively, are shown. The bottom of the energy bands, indicated by the straight lines, thus corresponds to the height of the potential which the waves have to overcome before they become propagating. This explains why we see four steps in the conductance in Figure G.1 **(a)-(d)**. When all the perturbation terms are taken into consideration, the four-fold degeneracy is completely broken, yielding four separated energy bands; as a result four effective potentials appear. When the energy is increased in the simulations, which in an experiment corresponds to tuning a back-gate which move the energy bands and thus vary the size of the potentials, the channels are opened one at a time, in the sense that the potentials are overcome in a step-like manner and we see perfect conductance from the given channel, since there are no sources of scattering in the straight tube. From the conductance simulation in Figure G.1 we find that the steps occur right at the energetic tips of the potentials.

This may also explain why the change in conductance occurs in steps of $2\phi_0$ in Figure G.1
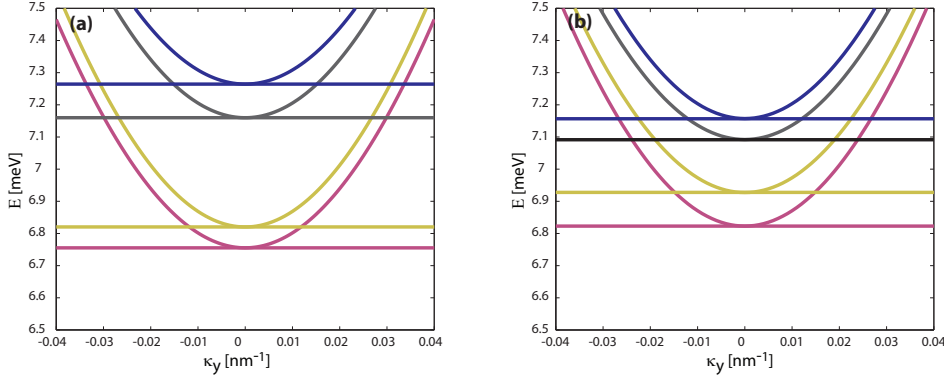
Figure 7.2: The four non-degenerate conduction bands with $B = 2$ T where **(a)** $\varphi = 30^{\circ}$ and **(b)** $\varphi = 60^{\circ}$. The straight lines indicate the energy where the steps 1 through 4 occur in Figure G.1 **(b)** and **(c)**, respectively. They match the bottom of the energy bands, such that the state belonging to a given band becomes propagating whenever the energy is tuned to this specific value for the band in question. This results in the quantized conductance.

(e) where the magnetic field is switched off. In this case the states within the Kramer doublets are two-fold degenerate, i.e. there are only two potential plateaus. Each band contribute with two channels thus yielding the two conductance steps of $2\phi_0$.

This reasoning may also explain why the lengths of the conductance plateaus are not the same for G.1 **(b)**-**(d)**. In Figure 7.2 it is clear that the energetic distances between the potentials are not the same; for **(a)** the first potential step (from band 1 to band 2) is smaller than the last potential step (band 3 to band 4), while the picture is reversed in **(b)**. However, in both cases the middle step (band 2 to band 3) is largest. This is consistent with the observed conductance patterns in Figure G.1 **(b)** and **(c)**. Thus rotation of the magnetic field toward $\varphi = 0$ lowers the first potential barrier, which is expressed in the conductance simulation through the fact that the first step occurs for a lower energy when $\varphi = 60^{\circ}$ than when $\varphi = 30^{\circ}$. However, the last conductance step get moved to a higher energy. This illustrates the effect of the Aharonov-Bohm and Zeeman terms on the energy bands. When φ decreases, the Aharonov-Bohm term increases due to the $B\cos(\varphi)$ dependence in eq. (5.11). The same is true for the Zeeman term proportional to $\cos(\varphi)S_3$ while the term proportional to $\sin(\varphi)S_1$ diminishes. The combined effect is that the two lower conductance bands are displaced downwards, while the upper two are displaced upwards. However, the displacements are not symmetric (see Figure 7.2), hence we develop the step patterns observed in the simulations.

It should be noted that while the steps are sharp for the transitions in Figure G.1 **(c)**-**(e)** there are noticeable fluctuations in the transmission and reflection at the transition $G = \phi_0 \rightarrow 2\phi_0$ in **(a)** and **(b)** such that the sum also fluctuates. This must be due to a numerical error. It may arise from the process of determining the correct eigenstates exactly at the point where the defined energy and the bottom of the conduction bands merge. However, it seemed strange that the fluctuations were only observed for magnetic fields which were close to being parallel to the tube and that they only appeared at some of the transitions. Further research is needed in order to determine the cause of this behavior, such that the code may be optimized in the future.

In addition, although we were able to simulate the conductance through a straight tube

with any number of channels open, whenever we performed the same scheme for bent tubes, the transmission and reflection showed fluctuations of up to several hundred orders of magnitude, which certainly cannot be physically correct. As a result, we were only able to study the bent tubes in the rather limited cases where all four incoming and transmissive channels were open.

Bent tubes. In general, the simulations yielded an increase in the transmission with increasing energy. This was expected and is in compliance with traditional scattering theory and experiments. The conductance plateaus and steps of ϕ_0 in a finite magnetic field agree with the experimental data reported in [11], in which a configuration very similar to the one used in Figure G.3 **(d)** (purple curve in Figure H.2 **(a)**) is investigated. However, in [11] the conductance steps were also ϕ_0 in the absence of a magnetic field. This was not seen in our simulations, where the steps were $2\phi_0$ (See Figure G.3 **(e)**), because of the degeneracy of states within the Kramer doublets described above.

As for the straight tube, the observed steps and plateaus in the conductance may be attributed to waves passing through potential barriers. However, for bent tubes the barriers are not uniform throughout the tube. When the tube is bending, φ' changes resulting in a changed Hamiltonian and consequently a displacement of the energy bands. If the displacement of the j'th band is sufficiently large, the corresponding j'th potential becomes larger than the energy of the initial state in the j'th band, which then becomes evanescent over some region, analogous to an imaginary eigenvalue λ_j in eq. (6.7). As a result, we see reflection. However, there is a finite probability of the wave passing through the barrier. Especially, if the distance over which λ_j is imaginary is short, compared to the length of the tube, and the conduction band containing the j'th state is close to the given Fermi energy, corresponding to a low, thin potential barrier, the transmission will be nearly perfect, giving rise to a conductance close to ϕ_0 from the j'th channel. The situation is illustrated in Figure 7.3 for four incoming waves with different energies. The low-energy wave (red) gets completely reflected since the evanescent wave in the barrier completely dies out, yielding zero transmission and as a consequence, zero conductance. For the intermediate-energy wave (blue) a portion of the wave gets reflected. But the evanescent wave survives the trip through the potential and thus gets partially transmitted yielding conductance in non-integer values of ϕ_0. The energy of the green wave is close to the top of the potential, thus we see nearly perfect transmission. For the high energy wave (yellow) reflection is negligible and the propagating wave is fully transmitted resulting in conductance of integer value ϕ_0.
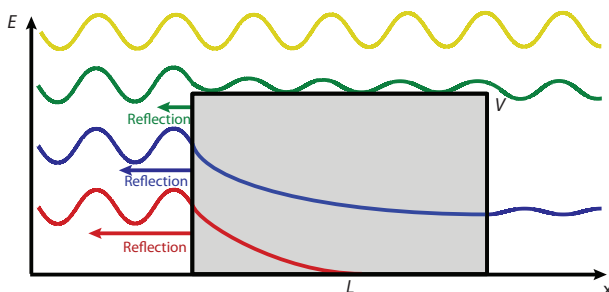

Figure 7.3: Scattering from a potential barrier of height V and width L. The low- and medium-energy waves (red) and (blue) are evanescent within the potential barrier. The red gets fully reflected, while a fraction of the blue gets transmitted. The green propagating wave is close to being fully transmitted. For the high-energy wave (yellow) reflection is negligible and the wave gets fully transmitted. Not to scale.

In Figure I.1 the bottom of the four conductance bands are displayed as a function of the location along the tube for the geometries used in the simulations in Figure G.2,G.3 **(b)-(d)**

(i.e. the configurations given in Figure H.1,H.2 **(a)**). In the above reasoning, the curves thus correspond to the potential barriers which the waves have to pass through. The dimensions of the potentials are directly linked to the degree of bending. This explains why only a partial step of approximately $0.4\phi_0, 0.5\phi_0$ appears in Figure G.2,G.3 **(b)**. Since the energy of the incoming waves are close to the top of the largest potential in Figure I.1 **(a)**, only a small fraction gets reflected. As the energy is increased all solutions become propagating and reflection becomes negligible and we thus see perfect transmission and conductance.

For the geometries used in Figure G.2 **(c)**,**(d)** and Figure G.3 **(c)**,**(d)**,**(f)**, however, the potentials become large enough that one of the states completely dies out. As a result only three states are transmitted yielding the observed conductance of $3\phi_0$.

It is interesting that an additional conductance step is seen from $G \approx 2\phi_0 \rightarrow 3\phi_0$ in Figure G.3 **(d)**. The difference between the tube configuration in this simulation and the hill-like one used in simulation G.2 **(d)**, which only shows one conductance step, is that the harmonically shaped tube has an extra bend upwards (compare the topology in Figure H.2 and Figure H.1 corresponding to the purple lines). This results in an extra potential bump at 250 to 450 nm (compare Figure I.1 **(e)** and **(f)**), such that the waves effectively see a double potential barrier. An incoming wave, which is transmitted through the first potential bump, may die out when moving through the second, resulting in the observed conductance plateau at $2\phi_0$. This may also explain why this step is absent in Figure G.3 **(f)**, where the magnetic field is 7 T and why no steps are seen when B = 5 T, since the displacements of the energy bands in this case are smaller, thus resulting in smaller potential bumps. The result is that for the energies swept in the simulations only one channel dies out, yielding the conductance of $3\phi_0$ for B = 7T, while for B = 5T none die out and $G = 4\phi_0$. It should be noted, however, that transmission is not additive, and in an accurate description we need to treat the two potentials as a whole.

This may explain why we do not see a complete extinction of the conductance for the ω shaped tube in Figure G.4 **(c)**. The potential seen by an incoming wave corresponds to two of the potentials in Figure I.1 **(e)** placed in tandem, such that there are effectively four potential barriers. One might think that the wave would get completely reflected for energies where Figure G.3 **(d)** showed conductance of $2\phi_0$, however this is not the case. The overall appearance of the conductance curve resembles that of Figure G.3 **(b)**, however the step from $G \approx 2\phi_0 \rightarrow 3\phi_0$ is much sharper in Figure G.4 **(c)** and occurs at a higher energy. In addition dips and peaks in the conductance appear. Peaks in the conductance are also observed for staircase tube. At energies 8.45 meV and 8.4 meV an increase in the conductance for the configurations with the intermediate straight segment being 50 and 100 nm, respectively, is visible. In the latter case the effect more pronounced.

The potential seen by a waves in this case corresponds to two spatially separated symmetric potential barriers, since the tube is build from linking two hill-like bent tubes (see Figure I.1 **(f)**) through an intermediate straight section of length 50 nm and 100 nm for Figure G.2 **(e)** and **(f)**, respectively. It can be shown that for a spatially separated series of two symmetric 1-D potentials, at certain energies, full transmission occurs even though the transmission through the individual barriers are small [14, p. 537]. In our simulations we did not see full transmission, however the peaks correspond to an enhancement of the transmission.

The effect arises because the waves in between the potentials travel back and forward constantly getting reflected and transmitted and thus acquire a phase. The double barrier system is illustrated in Figure 7.4. I and R denote incoming and reflected waves, while T denote the transmitted waves. The red waves denote waves in between the potential barriers

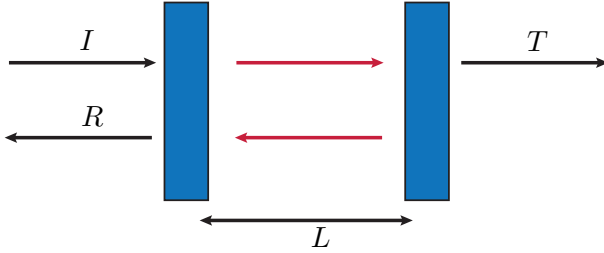which travel back and forward. At resonance, the waves will propagate in phase yielding a

Figure 7.4: Scattering from two symmetric barriers placed at a distance L from each other. I denote incoming waves, R indicate reflected waves while T denote transmitted waves. The waves travel back and forward in between the potentials (red) and acquire a phase. At resonance they propagate in phase, yielding enhanced transmission.

greatly enhanced transmission (conductance) due to constructive interference. This is called *resonant tunneling*. The energies at which resonance effect occurs depend on the distance between the potentials, since this affects the phase that the waves acquire. This dependence is visible in the conductance simulation, since the observed peaks occur for different energies in Figure G.2 **(e)** and **(f)**.

The effect carries over to the situation in Figure G.4, where the waves effectively see a potential consisting of four subsequent bumps; i.e. two pairs of the potential landscape shown in Figure I.1 **(e)** places in tandem. However, the system becomes much more complicated in this case. Nevertheless, for certain energies we would expect to see increase (decrease) in the transmission, whenever the waves are close to being in (out of) phase, expressed as the observed peaks and dips in the conductance, respectively.

A very important element of the results which has so far been left out of the discussion, is the failure of the transmission and reflection to equal the expected value of 4, i.e. the number of open incoming channels. The effect is more pronounced for the harmonically and ω-shaped tubes for large-bending in the low energy regime. However, in all simulations the sum converges towards the expected value as the energy is increased. That the sum, for one does not equal 4, and secondly fails to be constant (e.g. see the oscillations in the red curve for energies 8 meV to 8.5 meV in Figure G.3 **(d)** and **(f)** and Figure G.4 **(b)** and **(c)**) is of course not physically compatible and must be attributed to an error in the simulation scheme. The error may arise because of the crossings of the non-degenerate bands as the electrons move along the tube. E.g. the red and blue bands cross in Figure I.1 **(c)** and **(e)**. Because the script does not explicitly take into consideration which band a given state belongs to (during the integration through the tube) errors may occur on this account. This reasoning may explain why the effect is not as pronounced for the small bend tubes, since none or only two of the bands cross in this case. However, a more elaborate simulation scheme which keeps track of which states belong to which bands is needed to determine if this is indeed the cause of the error.

8   Perspectives

Although the simulations showed problems presumably attributable to numerical issues or limitations in the code, interesting phenomena emerged from the study; the theoretical model was able to account for the conductance steps of e^2/h, which were previously reported for a bent nanotube. In addition, we saw indication of resonant tunneling for the staircase and ω shaped tubes. However, fine-tuning of the code is still needed. The most critical issues are the sum of the reflection and transmission not equaling the number of channels and the

failure to study bent tubes in which not all channels are open. The solution might be to keep track of band numbers and corresponding eigenstates. If the issues are sorted out, an obvious next step would be to simulate the conductance for a bent tube with a magnetic field of varying angle and strengths. Additionally, one may investigate other tube geometries, e.g. conformations where all incoming channels are open while one or more transmissive channels are closed. Since the bachelor thesis has a finite time span, the completion of this work must be postponed to a future project.

In a future study is would also be interesting to take into account additional interactions in the bent CNT Hamiltonian. E.g. the effect of phonon interactions and temperature are potential candidates. Finally, as noted in the introduction, few measurements focusing on bent nanotubes are available. It will thus be interesting to see how the theoretical predictions match the experimental data, when an in-depth study of the electronic properties of bent tubes is reported.

9 Conclusion

Through a tight-binding model of graphene and the use of periodic boundary conditions an effective Hamiltonian for the unperturbed carbon nanotubes was established. Inclusion of perturbative effects from a magnetic field, spin-orbit coupling and curvature induced hybridizations yielded an effective Hamiltonian leading to a breaking of the four-fold degeneracy. Subsequently the Hamiltonian was extended to bent nanotubes. On the basis of this Hamiltonian an integration routine for determining the transmission and reflection as a function of the bending was developed. Following the Landauer formula the conductance for a bent tube could be determined.

Five geometries; straight, hill-like, staircase, harmonically and ω-shaped tubes were investigated. Some of the simulations showed unphysical fluctuations in the transmission and reflection, which was concluded to be due to numerical errors. However, many interesting phenomena emerged from the study. In the presence of a magnetic field conductance steps of integer values of the conductance quantum e^2/h appeared, reflecting the complete splitting of the energy bands. The observed steps have been reported in a previous experimental study of bent nanotubes [11]. In the absence of a magnetic field we observed integer steps of $2e^2/h$ in the conductance, which was expected due to the degeneracy of the states within the Kramer doublets. In addition for the staircase and ω we saw indications of resonant tunneling which were explained by regarding the bending of the tube as waves traveling through effective potential barriers. It will be interesting to see how these theoretical will predictions match the experimental data, when measurements on these tube geometries are reported.

A   Tight-binding approximation for the energy dispersion for the π-band of graphene

The tight binding approximation is based on the method of constructing the total wavefunction as a linear combination of localized atomic wavefunctions of the atoms within the lattice. The Hamiltonian for a single electron in the potential of all the carbon atoms in graphene is given by

$$\mathcal{H} = \mathcal{H}_{\text{kin}} + \sum_{\mathbf{R}} [V_{\text{at}}(\mathbf{r} - \mathbf{R}_A - \mathbf{R}) + V_{\text{at}}(\mathbf{r} - \underbrace{(\mathbf{R}_A + \mathbf{d})}_{\mathbf{R}_B} - \mathbf{R})], \tag{A.1}$$

where the kinetic part is as usual $\hat{p}^2/2m_e$ and $\mathbf{R}_A$ and $\mathbf{R}_B$ denote the position of atom A and B, respectively. From the periodicity of the lattice we expect the wavefunctions to be described by Bloch functions. It can be shown that any Bloch function may be written in the form

$$\psi_{\mathbf{k}}(\mathbf{r}) = \frac{1}{\sqrt{N}} \sum_{\mathbf{R}}^{N} e^{i\mathbf{k}\cdot\mathbf{R}} \phi(\mathbf{r} - \mathbf{R}) \tag{A.2}$$

where ϕ are *Wannier functions*, which are not necessarily exact atomic wavefunctions, but often can be approximated to be so [23, 12]. It is clear that ψ fulfills Bloch's theorem, i.e. $\psi(\mathbf{r} + \mathbf{R}) = e^{i\mathbf{k}\cdot\mathbf{R}}\psi(\mathbf{r})$, with the sum taken over all sites. Taking into account that each unit cell contains two atoms, we adopt superpositions of the Wannier functions, such that $\phi(\mathbf{r}) = \alpha\phi_A(\mathbf{r}) + \beta\phi_B(\mathbf{r})$, where ϕ_A and ϕ_B are approximated as the p_z-orbitals on atom A and B, respectively. When looking separately at the two sublattices and letting $\mathbf{d}$ denote the vector connecting A and B atoms, the total wavefunction can thus be written [23, p. 186]

$$\psi_{\mathbf{k}}(\mathbf{r}) = \frac{1}{\sqrt{N}} \sum_{\mathbf{R}_A} e^{i\mathbf{k}\cdot\mathbf{R}_A} (\alpha\phi_A(\mathbf{r} - \mathbf{R}_A) + \beta\phi_B(\mathbf{r} - \mathbf{R}_A - \mathbf{d}))$$

$$= \alpha\frac{1}{\sqrt{N}} \sum_{\mathbf{R}_A} e^{i\mathbf{k}\cdot\mathbf{R}_A} (\phi_A(\mathbf{r} - \mathbf{R}_A)) + \beta\frac{1}{\sqrt{N}} \sum_{\mathbf{R}_B} e^{i\mathbf{k}\cdot(\mathbf{R}_B - \mathbf{d})} \phi_B(\mathbf{r} - \mathbf{R}_B)$$

$$= \alpha\Phi_{A,\mathbf{k}}(\mathbf{r}) + \beta\Phi_{B,\mathbf{k}}(\mathbf{r}) \tag{A.3}$$

where each of the sums are taken over all the unit cells in graphene, i.e. $\sum_{\mathbf{R}_A} = \sum_{\mathbf{R}_B} = N$. The atomic orbitals on each site are normalized, hence the total wavefunction is almost normalized, $|\langle\psi_{\mathbf{k}}|\psi_{\mathbf{k}}\rangle|^2 \approx 1$, if the overlap $\langle\phi(\mathbf{r} - \mathbf{R}_A)|\phi(\mathbf{r} - \mathbf{R}_B)\rangle$ is small.

Finding the eigenvalues and eigenfunctions is done in the usual way by solving the Schrödinger equation

$$\mathcal{H}\psi_{\mathbf{k}}(\mathbf{r}) = E_i(\mathbf{k})\psi_{\mathbf{k}}(\mathbf{r}) \tag{A.4}$$

which can be recast in matrix notation when we focus on the subset defined above. Multiplying from the left by $\psi_k^*(r)$, followed by integration over all space, results in the equation [13]

$$\begin{pmatrix} \mathcal{H}_{AA} & \mathcal{H}_{AB} \\ \mathcal{H}_{BA} & \mathcal{H}_{BB} \end{pmatrix} \begin{pmatrix} \alpha \\ \beta \end{pmatrix} = E_i(\mathbf{k}) \begin{pmatrix} S_{AA} & S_{AB} \\ S_{BA} & S_{BB} \end{pmatrix} \tag{A.5}$$

where $\mathcal{H}$ and $\mathcal{S}$ are called the *transfer integral* and *overlap integral* matrices, respectively. The matrix components are thus defined

$$\mathcal{H}_{ij}(\mathbf{k}) \equiv \langle\Phi_{i,\mathbf{k}}|\mathcal{H}|\Phi_{j,\mathbf{k}}\rangle \quad \text{and} \quad \mathcal{S}_{ij} \equiv \langle\Phi_{i,\mathbf{k}}|\Phi_{j,\mathbf{k}}\rangle. \tag{A.6}$$

From symmetry considerations the two diagonal terms of the transfer integral matrix are equivalent since the two sublattices only differ by a translation in space. These indices, where $i = A, B$, are determined in the following way

$$
\begin{aligned}
\mathcal{H}_{ii} &= \langle \Phi_{i,\mathbf{k}} | \mathcal{H} | \Phi_{i,\mathbf{k}} \rangle \\
&= \frac{1}{N} \sum_{\mathbf{R}_i} \sum_{\mathbf{R}'_i} e^{i(R-R')} \langle \phi_i(\mathbf{r} - \mathbf{R}_i) | \mathcal{H} | \phi_i(\mathbf{r} - \mathbf{R}'_i) \rangle \\
&= \frac{1}{N} \sum_{\mathbf{R}_i} \epsilon_0 = \epsilon_0,
\end{aligned}
\tag{A.7}
$$

since we only consider nearest neighbors atoms, which all belong to the other sublattice. In other words we neglect terms for which $\mathbf{R}_i > \mathbf{R}'_i$ and retain only $\mathbf{R}_i = \mathbf{R}'_i$ and define $\epsilon_0 \equiv \langle \phi_i(\mathbf{r} - \mathbf{R}_i) | \mathcal{H} | \phi_i(\mathbf{r} - \mathbf{R}'_i) \rangle$. In a similar manner, the off-diagonal term $\mathcal{H}_{AB}$, is calculated

$$
\begin{aligned}
\mathcal{H}_{AB} &= \frac{1}{N} \sum_{\mathbf{R}_B} \sum_{\mathbf{R}_A} e^{i\mathbf{k} \cdot (\mathbf{R}_B - \mathbf{d} - \mathbf{R}_A)} \langle \phi_A(\mathbf{r} - \mathbf{R}_A) | \mathcal{H} | \phi_B(\mathbf{r} - \mathbf{R}_B) \rangle \\
&= \frac{1}{N} \sum_{\mathbf{R}_A} \left(1 + e^{-i\mathbf{k} \cdot \mathbf{a_1}} + e^{-i\mathbf{k} \cdot \mathbf{a_2}} \right) (-\gamma_0) \\
&= -\gamma_0 \left(1 + e^{-i\mathbf{k} \cdot \mathbf{a_1}} + e^{-i\mathbf{k} \cdot \mathbf{a_2}} \right) \\
&= -\gamma_0 \boldsymbol{\alpha}(\mathbf{k})
\end{aligned}
\tag{A.8}
$$

when we take into consideration only the three neighboring atoms ($\mathbf{R}_A = \mathbf{R}_B - \mathbf{d}$, $\mathbf{R}_A = \mathbf{R}_B - \mathbf{d} + \mathbf{a_1}$ and $\mathbf{R}_A = \mathbf{R}_B - \mathbf{d} + \mathbf{a_2}$). Due to the symmetry of the lattice, the transfer integral $-\gamma_0$, which is defined $\langle \phi_A(\mathbf{r} - \mathbf{R}_A) | \mathcal{H} | \phi_B(\mathbf{r} - \mathbf{R}_B) \rangle$ is equivalent in all three cases and is assumed to be real. From the Hermiticity of $\mathcal{H}$ we conclude that $\mathcal{H}_{BA} = \mathcal{H}_{AB}^*$.

The diagonal terms of the overlap integral matrix are set to unity since $\mathcal{S}_{ii} = \langle \Phi_{i,\mathbf{k}} | \Phi_{i,\mathbf{k}} \rangle = 1$, $(i = A, B)$ in the nearest neighbor approximation, when assuming that the atomic wavefunction is normalized [13, p. 24]. The off-diagonal terms are found in the same way as the transfer integral, and we get $\mathcal{S}_{AB} = \mathcal{S}_{BA}^* = \gamma_1 \boldsymbol{\alpha}(\mathbf{k})$, with γ_1 called the overlap integral, defined $\langle \phi_A(\mathbf{r} - \mathbf{R}_A) | \phi_B(\mathbf{r} - \mathbf{R}_B) \rangle$. For graphene table values are $\gamma_0 = 3.033$ and $\gamma_1 = 0.129$ [13, p. 32].

Finding the eigenvalues now corresponds to solving the secular equation $\det[\mathcal{H} - E\mathcal{S}] = 0$, which yields the following two eigenenergies

$$
E_+(\mathbf{k}) = \frac{\epsilon_0 + \gamma_0 |\boldsymbol{\alpha}(\mathbf{r})|}{1 - \gamma_1 |\boldsymbol{\alpha}(\mathbf{r})|} \text{ and } E_-(\mathbf{k}) = \frac{\epsilon_0 - \gamma_0 |\boldsymbol{\alpha}(\mathbf{r})|}{1 + \gamma_1 |\boldsymbol{\alpha}(\mathbf{r})|}.
\tag{A.9}
$$

Since each atomic orbital contributes with one electron, i.e. two electrons pr unit cell, $2N$ out of a total $4N$ possible states (due to spin) are filled, such that the valence band is completely filled. The top of the valance band, ϵ_0, thus corresponds to the Fermi energy, ϵ_F, whenever $\boldsymbol{\alpha}(\mathbf{k}) = 0$. This can be seen to occur when $\mathbf{k} = \mathbf{K}(\mathbf{K}')$, where $\mathbf{K}(\mathbf{K}')$ are given in eq. (3.4). Since we are free to choose the zero points of energy, we might as well set $\epsilon_0 = \epsilon_F = 0$.

In studying transport phenomena the relevant energy scale is thus the Fermi energy, since only electrons in the vicinity of this energy are capable of propagating through the crystal due to the Fermi-statistics and the Pauli principle. Therefore the relevant $\mathbf{k}$ scale is in the vicinity of the $\mathbf{K}(\mathbf{K})$-points, such that the energy is close to ϵ_0. Hence – assuming the overlap

integral is small the product $\gamma_1|\boldsymbol{\alpha}(\mathbf{r})| \ll 1$ in the vicinity of the Fermi energy and is thus neglected in the denominator. The Hamiltonian now take the simple form

$$\mathcal{H} = \begin{pmatrix} 0 & \mathcal{H}_{AB} \\ \mathcal{H}^*_{AB} & 0 \end{pmatrix} = \begin{pmatrix} 0 & -\gamma_0\boldsymbol{\alpha}(\mathbf{k}) \\ -\gamma_0\boldsymbol{\alpha}(\mathbf{k})^* & 0 \end{pmatrix} \tag{A.10}$$

and the eigenenergies and eigenstates in the A,B-basis given by the p_z orbitals on each sublattice thus become

$$E_\pm(\mathbf{k}) = \pm\gamma_0|\boldsymbol{\alpha}(\mathbf{r})|, \quad \begin{pmatrix} \alpha \\ \beta \end{pmatrix}_\pm = \frac{1}{\sqrt{2}} \begin{pmatrix} \mp\frac{\boldsymbol{\alpha}(\mathbf{k})}{|\boldsymbol{\alpha}(\mathbf{k})|} \\ 1 \end{pmatrix}. \tag{A.11}$$

where

$$|\boldsymbol{\alpha}(\mathbf{k})| = \sqrt{3 + \cos(\mathbf{k} \cdot \mathbf{a}_1) + 2\cos(\mathbf{k} \cdot \mathbf{a}_2) + \cos(\mathbf{k} \cdot [\mathbf{a}_1 - \mathbf{a}_2])}$$
$$= \sqrt{1 + 4\cos\left(\frac{\sqrt{3}ak_x}{2}\right)\cos\left(\frac{ak_y}{2}\right) + 4\cos^2\left(\frac{ak_y}{2}\right)} \tag{A.12}$$

In Figure A.1 **(a)** the energy dispersion relation for graphene is plotted i **k**-space along with indication of the first Brillouin zone. We note that at the symmetry points, **K** and **K′**, the valence and conduction bands actually touch. Hence graphene is a metal even at low temperatures.

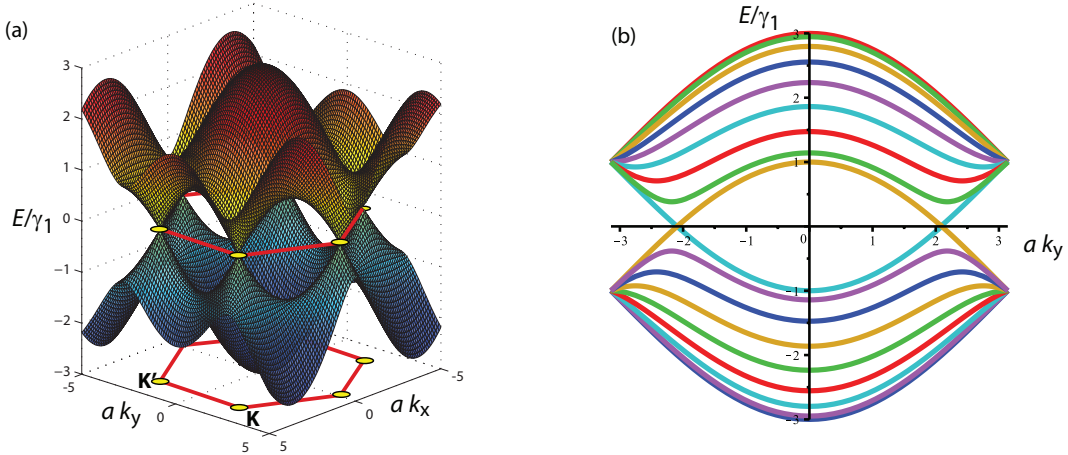**Figure A.1:** **(a)** Energy dispersion for graphene with the FBZ along with the **K** and **K′** points superimposed. The conductance and valence band touch at these high symmetry points. Since the fermi energy is taken to be the zeroth of energy, graphene is thus metallic. **(b)** Energy dispersion for an (4,4)-armchair tube. Since $N = 8$ eq. (3.9) eight valence and eight conduction bands can be seen.

Dispersion relation for armchair-tube. Since $k_C \parallel k_x$ for the armchair-tube the k_x values simply split up into the N allowed values, $\frac{2\pi n}{|\mathbf{C}|}$. Inserting into eq. (A.11) we get the dispersion relation depicted in Figure A.1 **(b)** for a (4,4)-tube. For all but the armchair tube, the wavevectors are not parallel and we need to project onto the CNT reference frame through a rotation. This rotation is described in Appendix C.

B Expansion of the dispersion relation around the K and K′ points

Most of the interesting physics regarding electronic transport happens around the Fermi energy. If we only take into consideration the first order contributions a much simpler expression for the dispersion relation is obtained. This approximation is only valid for **k**-values close to the **K** and **K′** points, with $\mathbf{K}(\mathbf{K'}) = \frac{2\pi}{a}(\frac{1}{\sqrt{3}}, \tau_3 \frac{1}{3})$, where $\tau_3 = 1(-1)$. I.e., writing $\mathbf{k} = \mathbf{K}(\mathbf{K'}) + \boldsymbol{\kappa}$ where $\boldsymbol{\kappa} = (\kappa_x, \kappa_y)$ we expand the energy dispersion relation around $\mathbf{K}(\mathbf{K'})$ for graphene. In the vicinity of the $\mathbf{K}(\mathbf{K'})$-points the energy is written $E_i(\mathbf{k}) = \epsilon(\boldsymbol{\kappa}) = \pm\gamma_0|\boldsymbol{\alpha}(\mathbf{r})|$ since $E(\mathbf{K}(\mathbf{K'})) \equiv 0$. Formally carrying out the expansion of $\boldsymbol{\alpha}$ to first order we find that

$$
\boldsymbol{\alpha}(\mathbf{K}^{(')} + \boldsymbol{\kappa}) = \nabla\boldsymbol{\alpha}(\mathbf{k})|_{\mathbf{K}^{(')}} \cdot \boldsymbol{\kappa} = -\left(i\boldsymbol{\kappa}\cdot\mathbf{a}_1 e^{-i\mathbf{K}^{(')}\cdot\mathbf{a}_1} + i\boldsymbol{\kappa}\cdot\mathbf{a}_2 e^{-i\mathbf{a}_2\cdot\mathbf{K}^{(')}}\right)
$$

$$
= -\left\{i\frac{a}{2}\begin{pmatrix}\kappa_x\\\kappa_y\end{pmatrix}\cdot\begin{pmatrix}\sqrt{3}\\1\end{pmatrix}e^{-i\frac{2\pi}{a}(\frac{1}{\sqrt{3}},\tau_3\frac{1}{3})\cdot\frac{a}{2}(\sqrt{3},1)} + i\frac{a}{2}\begin{pmatrix}\kappa_x\\\kappa_y\end{pmatrix}\cdot\begin{pmatrix}\sqrt{3}\\-1\end{pmatrix}e^{-i\frac{2\pi}{a}(\frac{1}{\sqrt{3}},\tau_3\frac{1}{3})\cdot\frac{a}{2}(\sqrt{3},-1)}\right\}
$$

$$
= -\frac{\sqrt{3}a}{2}\left\{i(\kappa_x + \frac{1}{\sqrt{3}}\kappa_y)e^{-i\pi\left(1+\frac{\tau_3}{3}\right)} + i(\kappa_x - \frac{1}{\sqrt{3}}\kappa_y)e^{-i\pi\left(1-\frac{\tau_3}{3}\right)}\right\}
$$

$$
= \frac{\sqrt{3}a}{2}\left\{i\kappa_x\left[e^{i\pi\frac{\tau_3}{3}} + e^{-i\pi\frac{\tau_3}{3}}\right] + i\frac{1}{\sqrt{3}}\kappa_y\left[e^{i\pi\frac{\tau_3}{3}} - e^{-i\pi\frac{\tau_3}{3}}\right]\right\}
$$

$$
= \frac{\sqrt{3}a}{2}\left\{i\kappa_x 2\cos\left(\pi\frac{\tau_3}{3}\right) - \frac{1}{\sqrt{3}}i\kappa_y 2i\sin\left(\pi\frac{\tau_3}{3}\right)\right\}
$$

$$
= \frac{\sqrt{3}a}{2}\left\{i\kappa_x 2\frac{1}{2} + \frac{2}{\sqrt{3}}\kappa_y\tau_3\frac{\sqrt{3}}{2}\right\}
$$

$$
= \frac{\sqrt{3}a}{2}\left(i\kappa_x + \tau_3\kappa_y\right). \tag{B.1}
$$

Following the definition, $\mathcal{H}_{AB} = -\gamma_0\frac{\sqrt{3}a}{2}\left(i\kappa_x + \tau_3\kappa_y\right)$, the effective Hamiltonian of graphene, when leaving the τ_3 as an entry corresponding to the $\mathbf{K}(\mathbf{K})$, is thus written in the following way

$$
\mathcal{H} = \begin{pmatrix} 0 & -\gamma_0\frac{\sqrt{3}a}{2}\left(i\kappa_x + \tau_3\kappa_y\right) \\ -\gamma_0\frac{\sqrt{3}a}{2}\left(-i\kappa_x + \tau_3\kappa_y\right) & 0 \end{pmatrix}. \tag{B.2}
$$

The eigenenergies can thus be found from $\epsilon(\boldsymbol{\kappa})^2 = |\mathcal{H}_{AB}|^2$ (which can also be seen from (A.11)). Since $|\boldsymbol{\alpha}(\mathbf{K} + \boldsymbol{\kappa})| = \frac{\sqrt{3}a}{2}\sqrt{\kappa_x^2 + \kappa_y^2} = \frac{\sqrt{3}a}{2}|\boldsymbol{\kappa}|$ the energy dispersion (A.9) expanded around the $\mathbf{K}(\mathbf{K'})$-points thus becomes

$$
\epsilon(\boldsymbol{\kappa}) = \pm\left(\frac{-\gamma_0\sqrt{3}a}{2}\right)|\boldsymbol{\kappa}|. \tag{B.3}
$$

Whenever one talks about single electrons with definite momentum one actually needs to consider a narrow range of k's in k-space which results in a relatively broad span of the spatial part of the wavefunction thus demanding a wave packet. It can be shown that the velocity of such a wave packet is given $\mathbf{v} = \hbar^{-1}\partial\epsilon/\partial\mathbf{k}$ [15, p. 415]. We see that the energy dispersion is independent of direction, only on magnitude of $\boldsymbol{\kappa}$ such that the velocity, which

in the vicinity of the Fermi energy, corresponds to the Fermi velocity is given by

$$v_F = \frac{-\gamma_0 \sqrt{3}a}{2\hbar}. \tag{B.4}$$

We are then capable of providing an approximative solution for the dispersion relation and eigenstates, within the vicinity of the **K**-points:

$$\epsilon_\pm(\boldsymbol{\kappa}) = \pm\hbar v_F|\boldsymbol{\kappa}|, \quad \begin{pmatrix} \alpha \\ \beta \end{pmatrix}_\pm = \frac{1}{\sqrt{2}}\begin{pmatrix} \mp e^{i\beta} \\ 1 \end{pmatrix}, \tag{B.5}$$

where $\beta = \arg(\boldsymbol{\alpha}(\mathbf{k}))$ since $\boldsymbol{\alpha}(\mathbf{k}) = |\boldsymbol{\alpha}(\mathbf{k})|\exp\{i\arg[\boldsymbol{\alpha}(\mathbf{k})]\}$.

C   Rotation of the graphene Hamiltonian into the CNT reference frame

From Figure 3.1 **(a)** we see that the graphene Hamiltonian eq. (3.11) given in the (x, y)-coordinate system compared to the CNT unit vectors is given

$$\mathcal{H} = \hbar v_F \begin{pmatrix} 0 & (i\kappa_x + \tau_3\kappa_y)\, e^{-i\tau_3\eta} \\ (-i\kappa_x + \tau_3\kappa_y)\, e^{i\tau_3\eta} & 0 \end{pmatrix}. \tag{C.1}$$

This follows from the observation that

$$\begin{pmatrix} \kappa_x \\ \kappa_y \end{pmatrix} = \begin{pmatrix} \cos\eta & -\sin\eta \\ \sin\eta & \cos\eta \end{pmatrix} \begin{pmatrix} \kappa_C \\ \kappa_T \end{pmatrix}, \tag{C.2}$$

such that the matrix elements of the Hamiltonian become

$$\mathcal{H}_{12} = \hbar v_F \left[i(\cos\eta\,\kappa_C - \sin\eta\,\kappa_T) + \tau_3(\sin\eta\,\kappa_C + \cos\eta\,\kappa_T \right] \tag{C.3}$$

$$\mathcal{H}_{21} = \hbar v_F \left[-i(\cos\eta\,\kappa_C - \sin\eta\,\kappa_T) + \tau_3(\sin\eta\,\kappa_C + \cos\eta\,\kappa_T) \right]. \tag{C.4}$$

Collecting the like-terms we thus find

$$\mathcal{H}_{12} = \hbar v_F \left[i\kappa_C(\cos\eta - i\tau_3\sin\eta\,\kappa_C) + \tau_3\kappa_T(\cos\eta\,\kappa_T - \tau_3\sin\eta\,\kappa_T) \right] \tag{C.5}$$

$$\mathcal{H}_{21} = \hbar v_F \left[-i\kappa_C(\cos\eta + i\tau_3\sin\eta\,\kappa_C) + \tau_3\kappa_T(\cos\eta\,\kappa_T + \tau_3\sin\eta\,\kappa_T) \right]. \tag{C.6}$$

since $(\tau_3)^2 = 1$, which indeed gives us the Hamiltonian in eq. (C.1). Transforming the Hamiltonian into the reference frame of the CNT thus corresponds a to rotation of the (x, y) coordinate system through the angle η by means of the unitary rotation matrix

$$U = \begin{pmatrix} e^{i\tau_3\eta} & 0 \\ 0 & 1 \end{pmatrix} \tag{C.7}$$

with $\tau_3 = 1(-1)$ corresponding to the $\mathbf{K}(\mathbf{K}')$-point. The effective Hamiltonian, in the CNT coordinate system, thus becomes $\mathcal{H}_0 = \mathbf{U}\mathcal{H}\mathbf{U}^{-1}$ [6], i.e.

$$\mathcal{H}_0 = \hbar v_F \begin{pmatrix} 0 & i\kappa_C + \tau_3\kappa_T \\ -i\kappa_C + \tau_3\kappa_T & 0 \end{pmatrix} \tag{C.8}$$

Circumferential quantization   Here the full calculation of the quantization of the circumferential wavevector of the nanotube is given. The quantization condition from Bloch's theorem yields

$$\mathbf{k} \cdot \mathbf{C} = 2\pi n, \tag{C.9}$$

such that

$$2\pi n = \mathbf{k} \cdot \mathbf{C}$$
$$2\pi n = (\mathbf{K}(\mathbf{K}') + \boldsymbol{\kappa}) \cdot \mathbf{C}$$
$$2\pi n = \left[\frac{2\pi}{a} \begin{pmatrix} \frac{1}{\sqrt{3}} \\ \tau_3 \frac{1}{3} \end{pmatrix} + \kappa_C \frac{\mathbf{C}}{|\mathbf{C}|} + \kappa_T \frac{\mathbf{T}}{|\mathbf{T}|} \right] \cdot \mathbf{C}$$
$$2\pi n = \left[\frac{2\pi}{a} \begin{pmatrix} \frac{1}{\sqrt{3}} \\ \tau_3 \frac{1}{3} \end{pmatrix} \right] \cdot \left[n_1 \frac{a}{2} \begin{pmatrix} \sqrt{3} \\ -1 \end{pmatrix} + n_2 \frac{a}{2} \begin{pmatrix} \sqrt{3} \\ 1 \end{pmatrix} \right] + \kappa_C |\mathbf{C}|$$
$$2\pi n = \pi \left[n_1 (1 - \frac{\tau_3}{3}) + n_2 (1 + \frac{\tau_3}{3}) \right] + \kappa_C |\mathbf{C}|$$
$$\kappa_C = \frac{1}{2R} \left[2n - (n_1 + n_2) + \frac{\tau_3}{3}(n_2 - n_1) \right]. \tag{C.10}$$

where $R = |\mathbf{C}|/2\pi$. It is clear that the latter term is an integer if the equation $(n_2 - n_1) = 3N + \mu$ ($N \in \mathbb{Z}$) yields $\mu = 0$, while it is a non-integer for $\mu = \pm 1$. The second term, however, is always an integer since $(n_1 + n_2) \in \mathbb{Z}$. Absorbing all the integer values into m the quantized wavevector may be written

$$\kappa_C = \frac{1}{R} \left(m - \frac{\tau_3 \mu}{3} \right). \tag{C.11}$$

D   Rotation of the spin matrices

From the generator of rotation the spin-basis transformation from the global to the local coordinate system is given

$$\chi' = e^{i(\mathbf{S}\cdot\hat{n})\varphi'/2}\chi, \tag{D.1}$$

where $\hat{n}$ describes an arbitrary direction in the global coordinate system. Hence the local spin-basis is derived – with the global spin-basis defined

$$\chi_+ = \begin{pmatrix} 1 \\ 0 \end{pmatrix} \text{ and } \chi_- = \begin{pmatrix} 0 \\ 1 \end{pmatrix}, \tag{D.2}$$

i.e. $\chi = a\chi_+ + b\chi_-$ – by investigating the effect of the transformation on these basis vectors, which are the eigenvectors of S_3. This gives us

$$\chi'_+ = e^{i(\mathbf{S}\cdot\hat{n})\varphi'/2}\chi_+ \text{ and } \chi'_- = e^{i(\mathbf{S}\cdot\hat{n})\varphi'/2}\chi_-. \tag{D.3}$$

Thus, the 2×2 change of base matrix $e^{i(\mathbf{S}\cdot\hat{n})\varphi'/2}$ will now be derived. The generalized exponential operator is defined such that

$$e^{i(\mathbf{S}\cdot\hat{n})\varphi'/2} = \sum_{k=0}^{\infty}\frac{1}{k!}(i(\mathbf{S}\cdot\hat{n})\varphi'/2)^k = \sum_{k=0}^{\infty}\frac{1}{n!}\left(\frac{i\varphi'}{2}\right)^k(\mathbf{S}\cdot\hat{n})^k. \tag{D.4}$$

In order to be consistent with current notation we set the principle quantum axis in the direction of the tube ($\hat{y}$), such that

$$S_3 = S_{\hat{y}} \equiv \begin{pmatrix} 1 & 0 \\ 0 & -1 \end{pmatrix}. \tag{D.5}$$

$\mathbf{S}\cdot\hat{n} = S_i$ for $i = 1, 2, 3$ for $\hat{n}$ equal to $\hat{x}$, $\hat{z} = \hat{x} \times \hat{y}$, and $\hat{y}$ respectively, where

$$S_1 = \begin{pmatrix} 0 & 1 \\ 1 & 0 \end{pmatrix}, \quad S_2 = \begin{pmatrix} 0 & -i \\ i & 0 \end{pmatrix}, \quad S_3 = \begin{pmatrix} 1 & 0 \\ 0 & -1 \end{pmatrix}. \tag{D.6}$$

It can easily be shown that

$$(S_i)^n = \begin{cases} \mathbf{1}, & \text{for } n \text{ even} \\ S_i, & \text{for } n \text{ uneven} \end{cases} \tag{D.7}$$

Thus eq. (D.4) becomes

$$e^{i(\mathbf{S}\cdot\hat{n})\varphi'/2} = \sum_{\substack{k = 0, \\ \text{even}}}^{\infty}\frac{1}{k!}\left(\frac{i\varphi'}{2}\right)^k\mathbf{1} + \sum_{\substack{k = 1, \\ \text{uneven}}}^{\infty}\left(\frac{i\varphi'}{2}\right)^k(\mathbf{S}\cdot\hat{n})$$

$$= \mathbf{1}\sum_{\substack{k = 0, \\ \text{even}}}^{\infty}(-1)^{(n/2)}\frac{1}{k!}\left(\frac{\varphi'}{2}\right)^k + i(\mathbf{S}\cdot\hat{n})\sum_{\substack{k = 1, \\ \text{uneven}}}^{\infty}(-1)^{(n-1)/2}\frac{1}{k!}\left(\frac{\varphi'}{2}\right)^k. \tag{D.8}$$

The first and the latter sum is identified as $\cos(\varphi'/2)$ and $\sin(\varphi'/2)$, respectively. The change-of-base matrix is thus given

$$\mathbf{R} = \mathbf{1}\cos(\varphi'/2) + i(\mathbf{S}\cdot\hat{n})\sin(\varphi'/2). \tag{D.9}$$

For a rotation through the angle φ' around the $\hat{z}$ direction the matrix becomes

$$\mathbf{R}_{\hat{z}(\varphi')} = \begin{pmatrix} \cos(\varphi'/2) & \sin(\varphi'/2) \\ -\sin(\varphi'/2) & \cos(\varphi'/2) \end{pmatrix}. \tag{D.10}$$

With the given rotation, the spinor basis are transformed in the following way

$$\chi'_+ = \mathbf{R}_{\hat{z}(\varphi')}\chi_+ = \begin{pmatrix} \cos(\varphi'/2) & \sin(\varphi'/2) \\ -\sin(\varphi'/2) & \cos(\varphi'/2) \end{pmatrix}\begin{pmatrix} 1 \\ 0 \end{pmatrix} = \begin{pmatrix} \cos(\varphi'/2) \\ -\sin(\varphi'/2) \end{pmatrix}. \tag{D.11}$$

$$\chi'_- = \mathbf{R}_{\hat{z}(\varphi')}\chi_- = \begin{pmatrix} \cos(\varphi'/2) & \sin(\varphi'/2) \\ -\sin(\varphi'/2) & \cos(\varphi'/2) \end{pmatrix}\begin{pmatrix} 0 \\ 1 \end{pmatrix} = \begin{pmatrix} \sin(\varphi'/2) \\ \cos(\varphi'/2) \end{pmatrix}. \tag{D.12}$$

From linear algebra it is given, that if the transformation $f : \mathscr{H} \to \mathscr{H}$ is represented by the matrix $\mathbf{S}$ and $\mathbf{S}'$ in the old and new basis, respectively, then

$$\mathbf{S}' = \mathbf{R}\mathbf{S}\mathbf{R}^{-1}. \tag{D.13}$$

This allow us to determine the new operators $S'_i = \mathbf{S}\cdot\hat{i}'$ for $i = y, x, z$ in terms of the the old. For $\hat{y}$ we get the the primed operator in the following way

$$S'_{\hat{y}} = \mathbf{R}_{\hat{z}(\varphi')}S_{\hat{y}}\mathbf{R}^{-1}_{\hat{z}(\varphi')} \tag{D.14}$$

$$= \begin{pmatrix} \cos(\varphi'/2) & \sin(\varphi'/2) \\ -\sin(\varphi'/2) & \cos(\varphi'/2) \end{pmatrix}\begin{pmatrix} 1 & 0 \\ 0 & -1 \end{pmatrix}\begin{pmatrix} \cos(\varphi'/2) & \sin(\varphi'/2) \\ -\sin(\varphi'/2) & \cos(\varphi'/2) \end{pmatrix}^{-1}$$

$$= \begin{pmatrix} \cos(\varphi'/2) & \sin(\varphi'/2) \\ -\sin(\varphi'/2) & \cos(\varphi'/2) \end{pmatrix}\begin{pmatrix} \cos(\varphi'/2) & -\sin(\varphi'/2) \\ -\sin(\varphi'/2) & -\cos(\varphi'/2) \end{pmatrix} \tag{D.15}$$

$$= \begin{pmatrix} \cos^2(\varphi'/2) + \sin^2(\varphi'/2) & -2\sin(\varphi'/2)\cos(\varphi'/2) \\ -2\sin(\varphi'/2)\cos(\varphi'/2) & \sin^2(\varphi'/2) - \cos^2(\varphi'/2) \end{pmatrix}$$

$$= \begin{pmatrix} \cos(\varphi') & \sin(\varphi') \\ \sin(\varphi') & -\cos(\varphi') \end{pmatrix} = \sin(\varphi')S_1 + \cos(\varphi')S_3. \tag{D.16}$$

This can also be seen by expressing $\hat{y}'$ in terms of $\hat{y}$ and $\hat{x}$

$$\begin{aligned} \mathbf{S}\cdot\hat{y}' &= \mathbf{S}\cdot[\cos(\varphi')\hat{y} + \sin(\varphi')\hat{x}] \\ &= (S_1, S_2, S_3)\cdot(\sin(\varphi'), 0, \cos(\varphi')) \\ &= \sin(\varphi')S_1 + \cos(\varphi')S_3. \end{aligned} \tag{D.17}$$

An equivalent calculation yields the local spin-operator in the $\hat{x}'$ direction:

$$S'_x = \mathbf{S}\cdot[-\sin(\varphi')\hat{y} + \cos(\varphi')\hat{x}] = \cos(\varphi')S_1 - \sin(\varphi')S_3 \tag{D.18}$$

E Evaluation of the exponential operator

We write $\mathbf{A} = \mathbf{M}_0^{-1}(\mathbf{M}_1(\phi, \varphi') - E)$. Instead of attacking the problem directly and Taylor expanding the exponential operator to a desired order, we turn to the much more numerically robust procedure of matrix diagonalization. From Linear Algebra it is given that when $\mathbf{A}$ is diagonalizable, the operator can be written $\mathbf{A} = \mathbf{UDU}^{-1}$, where $\mathbf{D}$ is a diagonal matrix with the eigenvalues of $\mathbf{A}$ λ_j written in the diagonal and $\mathbf{U}$ is the matrix with the j'th column consisting of the normalized eigenvector corresponding to the j'th eigenvalue of $\mathbf{A}$. Applying the definition of the exponential operator,

$$e^{\mathbf{A}} = \sum_{n=0}^{\infty} \frac{1}{n!} \mathbf{A}^n, \tag{E.1}$$

to $\mathbf{A}' = iy'\mathbf{A} = iy'\mathbf{UDU}^{-1} = \mathbf{UD}'\mathbf{U}^{-1}$, with $\mathbf{D}' = iy'\mathbf{D}$, we find

$$e^{iy'\mathbf{A}} = \sum_{n=0}^{\infty} \frac{1}{n!} \left(\mathbf{UD}'\mathbf{U}^{-1}\right)^n = \sum_{n=0}^{\infty} \frac{1}{n!} \mathbf{UD}'^n \mathbf{U}^{-1}, \tag{E.2}$$

where in the the last step we have used that

$$\left(\mathbf{UD}'\mathbf{U}^{-1}\right)^n = \left(\mathbf{UD}'\mathbf{U}^{-1}\right)^{n-2} \left(\mathbf{UD}'\mathbf{U}^{-1}\mathbf{UD}'\mathbf{U}^{-1}\right) = \ldots = \mathbf{UD}'^n \mathbf{U}^{-1}, \tag{E.3}$$

because $\mathbf{U}^{-1}\mathbf{U} = \mathbf{1}$. Since $\mathbf{U}$ and $\mathbf{U}^{-1}$ are represented by finite-dimensional (8×8) matrices the operators are linear and bounded; hence they are continuous. This allows us to write

$$
\begin{aligned}
e^{\mathbf{U}\mathbf{D}'\mathbf{U}^{-1}} &= \sum_{n=0}^{\infty} \frac{1}{n!} \mathbf{U}\,\mathbf{D}'^{\,n}\mathbf{U}^{-1} \\
&= \lim_{N\to\infty} \sum_{n=0}^{N} \frac{1}{n!} \mathbf{U}\,\mathbf{D}'^{\,n}\,\mathbf{U}^{-1} \\
&= \lim_{N\to\infty} \left[\mathbf{U}\left(\sum_{n=0}^{N} \frac{1}{n!}\mathbf{D}'^{\,n}\right)\mathbf{U}^{-1}\right] = \mathbf{U}\lim_{N\to\infty}\left(\sum_{n=0}^{N}\frac{1}{n!}\mathbf{D}'^{\,n}\right)\mathbf{U}^{-1} \\
&= \mathbf{U}\left(\sum_{n=0}^{\infty}\frac{1}{n!}\mathbf{D}'^{\,n}\right)\mathbf{U}^{-1} \\
&= \mathbf{U}\,e^{\mathbf{D}'}\,\mathbf{U}^{-1}.
\end{aligned}
\tag{E.4}
$$

Calculation of the exponential operator applied to $\mathbf{D}'$ yields,

$$
\begin{aligned}
e^{\mathbf{D}'} &= \sum_{n=0}^{\infty}\frac{1}{n!}
\begin{pmatrix} iy'\lambda_1 & 0 & \cdots \\ 0 & \ddots & \vdots \\ \vdots & \cdots & iy'\lambda_8 \end{pmatrix}^n
= \lim_{N\to\infty}\sum_{n=0}^{N}
\begin{pmatrix} \frac{1}{n!}(iy'\lambda_1)^n & 0 & \cdots \\ 0 & \ddots & \vdots \\ \vdots & \cdots & \frac{1}{n!}(iy'\lambda_8)^n \end{pmatrix} \\
&= \begin{pmatrix} \lim_{N\to\infty}\sum_{n=0}^{N}\frac{1}{n!}(iy'\lambda_1)^n & 0 & \cdots \\ 0 & \ddots & \vdots \\ \vdots & \cdots & \lim_{N\to\infty}\sum_{n=0}^{N}\frac{1}{n!}(iy'\lambda_8)^n \end{pmatrix}.
\end{aligned}
$$

Taking the limit in the sum for $N \to \infty$ we get

$$
e^{\mathbf{D}'} = \begin{pmatrix} \sum_{n=0}^{\infty} \frac{1}{n!}(iy'\lambda_1)^n & 0 & \cdots \\ 0 & \ddots & 0 \\ \vdots & \cdots & \sum_{n=0}^{\infty} \frac{1}{n!}(iy'\lambda_8)^n \end{pmatrix}
$$

$$
= \begin{pmatrix} e^{iy'\lambda_1} & 0 & \cdots \\ 0 & \ddots & \vdots \\ \vdots & \cdots & e^{iy'\lambda_8} \end{pmatrix} = \mathcal{D}. \tag{E.5}
$$

F Walkthrough of the simulation routine

The program for determining the transmission and reflection of the bent tube is separated into three main parts:

1. Generation of the dispersion relation.

2. Define given Fermi energy and search for $\kappa_{y'}$, reduce dimensions if necessary

3. Integration though the bent tube followed by collection of the transmission and reflection.

The dispersion relation is found by sweeping the desired span of $\kappa_{y'}$ and calculating the eight eigenvalues (and eigenfunctions) of the Hamiltonian to that specific $\kappa_{y'}$. Whenever the conformation of the end of the tube differs from that of the beginning, the eigenfunctions and the eigenvalues also need to be found here.

The Fermi energy is then set to a given value, and a reverse search in the dispersion relation is initiated by finding the minimum energy difference between the four conduction band and the given fermi energy. This is done for both positive and negative $\kappa_{y'}$s through the build-in MATLAB command `[C,I]:min(abs(E-E(i))`, which returns the energetic difference `C` and the corresponding eigenfunction of band `i` with right and left going waves **a** and **b** respectively[9]. Since the `min` command was found to be accurate to within $\approx 10^{-9}$ eV, we set a threshold of 10^{-7} eV, in the sense that if `i` is greater than this value, the $\boldsymbol{\mu}_{ij}$ is filled with zeros. This is implemented in the script in the following way (for $\boldsymbol{\mu}_a$).

```
for j=1:1:4;
  if abs(E(i)-E)>1.0*10^(-7);
          mu_a(:,j)=0;
        else
            ''fill with eignvectors''
  end
end
```

If the configuration is different at the end of the tube, an analogous search is done here. Otherwise we set $\boldsymbol{\mu}_a = \boldsymbol{\mu}_c$.

The eigenfunction matrix is then reduced if necessary. This is done by controlling if an entire column is filled with zeros, meaning that the channel is closed. The procedure for the reduction is done via the following for-loop

```
 del=any(mu_a,1);               % Check if all entries in column is zero
m=0;                            % Reset counter
for i=1:1:4;                    % Run loop through the 4 eigenstates
    m=m+1;                      % Add to counter
    if del(i)==0;              % Enter loop for del if entry is zero
        mu_a(:,m)=[];          % Delete the correct entries
        m=m-1;                 % Move back one column
    else
```

---

[9]When studying the dispersion relation for realistic parameters, the gradient was always positive (negative) for $\kappa_y > 0 (< 0)$, such that we always associate waves traveling to the right (left) with $\kappa_y > 0 (< 0)$.

```
        mu_a(:,m)=mu_a(:,m);   % Do nothing
    end
 end
```

When the correct eigenfunctions are found, we integrate through the tube. This is done as described above by for each step finding the $\mathbf{U}\mathcal{D}\mathbf{U}^{-1}$ for the matrix $\mathbf{A}$ which changes as a function of the tube angle with respect to the global coordinates. The angle dependence is determined by parameterizing the curve, such that we always take the same step dy' in the translational direction, while varying the angle φ' accordingly. Following the full integration the scattering matrix is calculated in the following way by the Moore-Penrose inversions routine

```
 S=([mu_c -M*mu_b]'*[mu_c -M*mu_b])^(-1)*[mu_c -M*mu_b]'*M*mu_a
```

The transmission and reflection coefficients are gathered. The energy is then raised and the energy search and wavefunction integration is repeated.
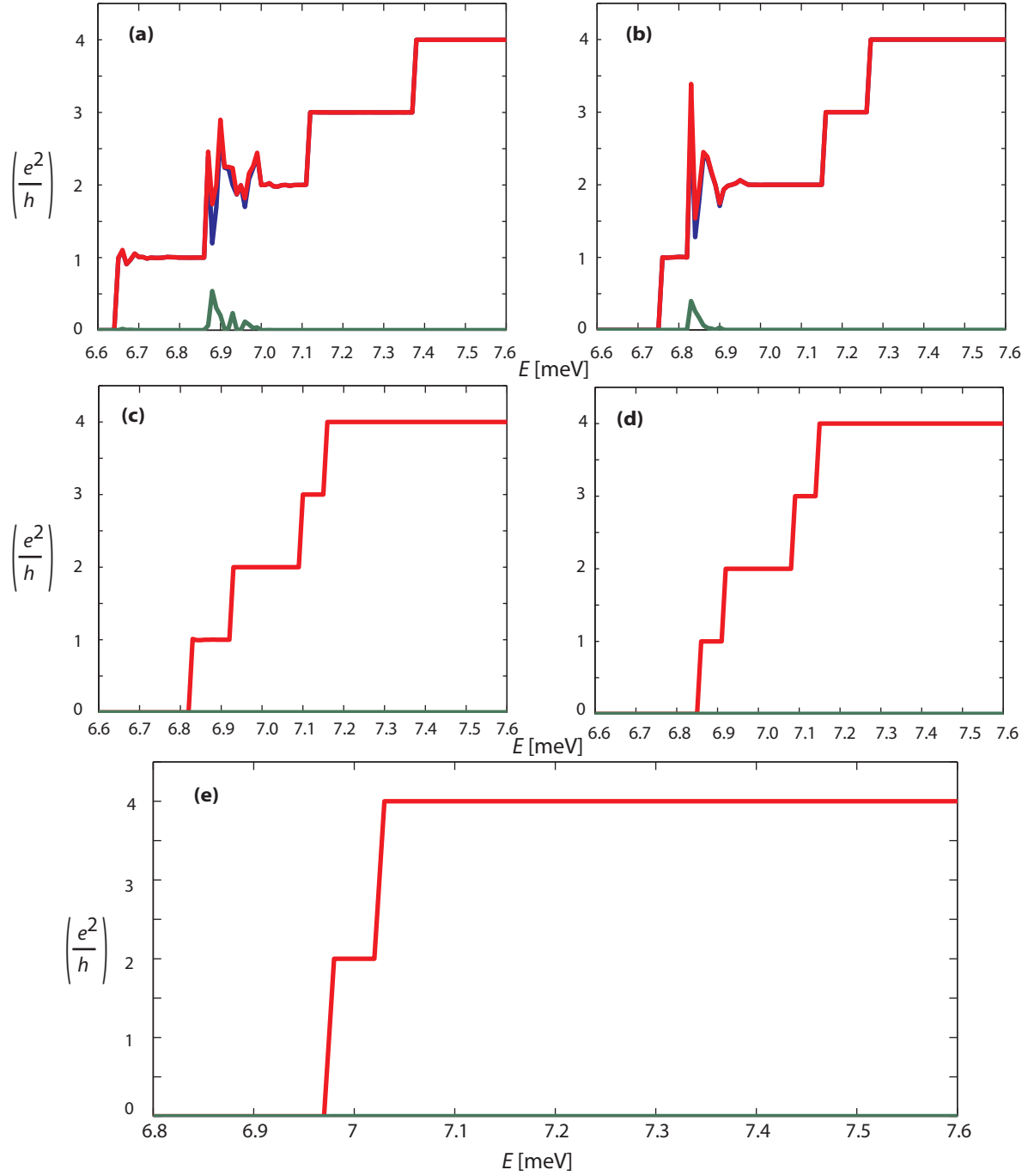
G   Results

Figure G.1: Transmission (conductance) as a function of energy for a straight tube of length 500 nm. The graphs correspond to different alignments of a 2T magnetic field, i.e. $\varphi = 0$, $\varphi = 30^{\circ}$, $\varphi = 60^{\circ}$ and $\varphi = 90^{\circ}$ for **(a)**-**(d)**, respectively. **(e)** shows the transmission (conductance) with the magnetic field switched off. The transmission and reflection are in arbitrary units, conductance is in units of the conductance quantum, e^2/h. Blue: Transmission (conductance); Green: Reflection; Red: Total. In **(c)**-**(b)** the blue line merge, because the reflection is negligible. See text for detailed discussion.
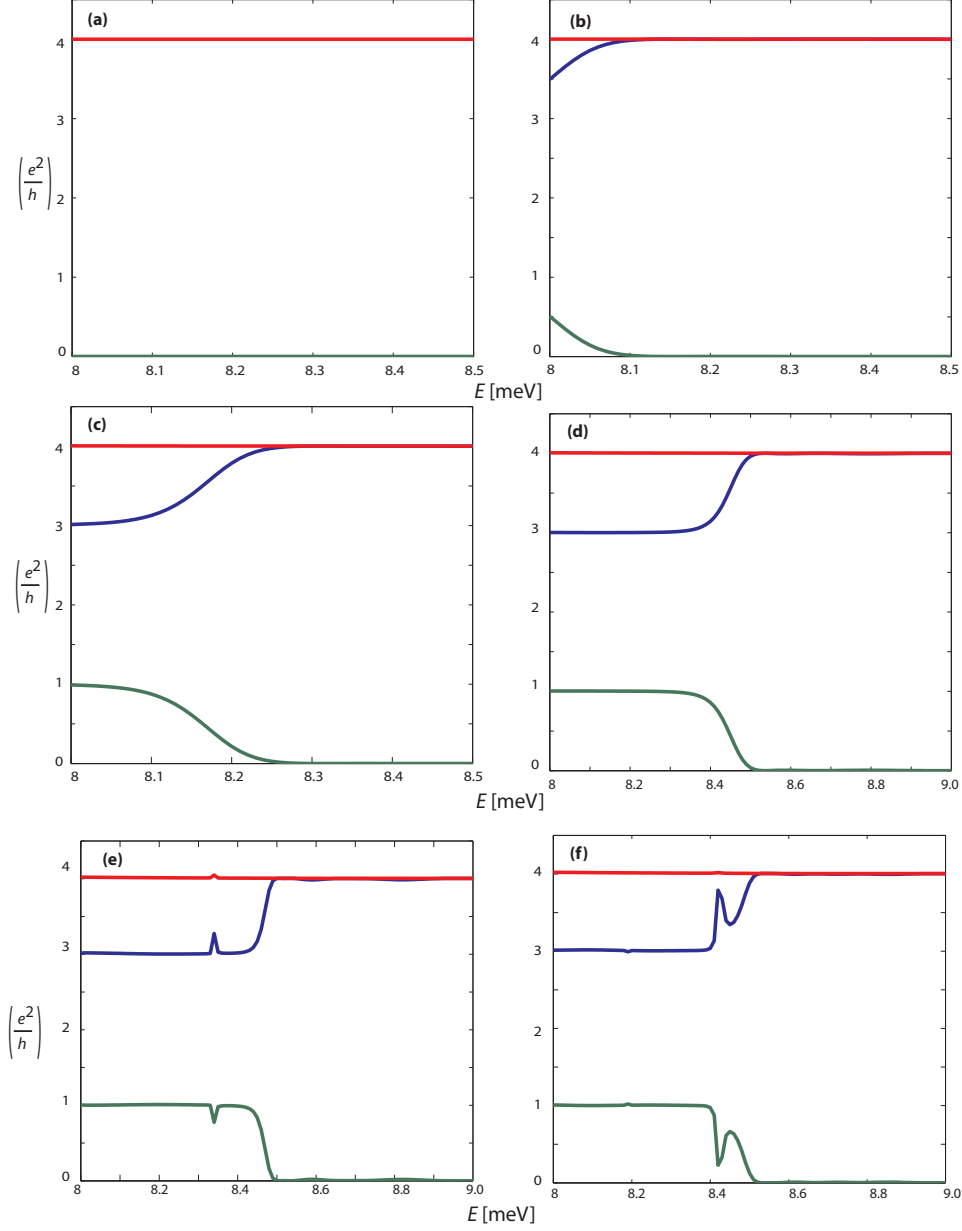
Figure G.2: Transmission (conductance) and reflection as a function of energy. The graphs correspond to different hill-like tube bendings of 0 nm, 20 nm, 40 nm and 100 nm, **(a)-(d)**, for a metallic zig-zag tube ($\mu = 0$, $\theta = 0$) with a radius of 2 nm in a magnetic field of 9 T aligned perpendicular to the straight tube. See Figure H.1 for details. **(e)** and **(f)**: Simulations for a tube constructed from connecting two 100 nm bending hill-like tubes through a straight segment of 50 and 100 nm, respectively. The transmission and reflection are in arbitrary units, while conductance is displayed in units of the conductance quantum, e^2/h. Blue: Transmission (conductance); Green: Reflection; Red: Total. See text for detailed discussion.
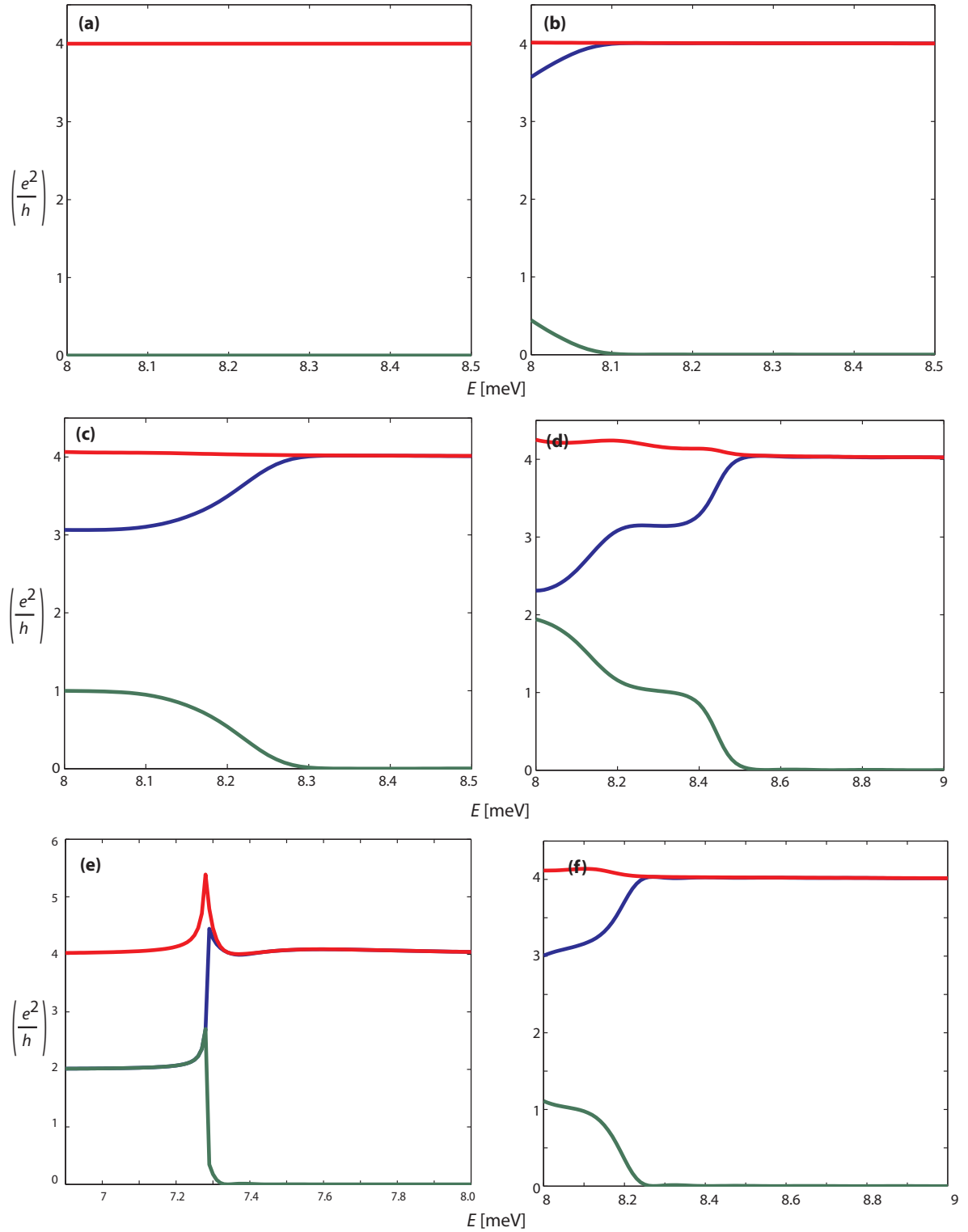
Figure G.3: Transmission (conductance) and reflection as a function of energy. The graphs correspond to different harmonically shaped tube bendings of 0 nm, 20 nm, 46 nm and 100 nm for **(a)**-**(d)** for a metallic zig-zag tube ($\mu = 0$, $\theta = 0$) with a radius of 2 nm in a magnetic field of 9 T aligned perpendicular to the straight tube. **(e)** and **(f)**: same as **(d)** but with a magnetic field of B=0 and B=5T, respectively. The transmission and reflection are in arbitrary units, while conductance is displayed in units of the conductance quantum, e^2/h. Blue: Transmission (conductance); Green: Reflection; Red: Total. See text for detailed discussion. In Figure H.2 the bending and angular dependece is illustrated.
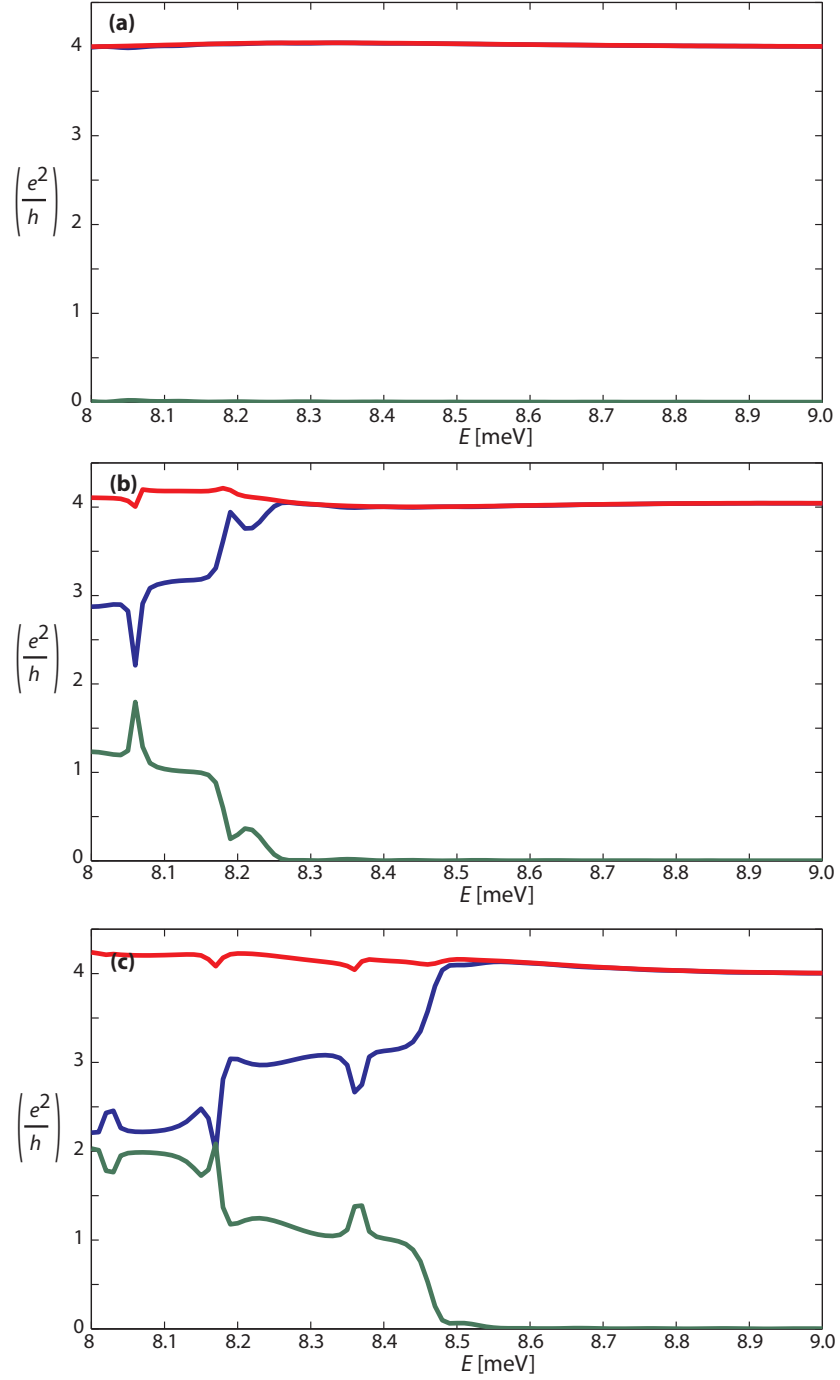
Figure G.4: Transmission (conductance) and reflection as a function of energy. The ω configuration corresponds to two harmonically shaped tubes with bending of 100 nm (Figure H.2 purple curves) placed in tandem. The graphs show simulation for a magnetic field of 5,7 and 9 T aligned perpendicular to the tube for **(a)**, **(b)** and **(c)**, respectively. The transmission and reflection are in arbitrary units, while conductance is displayed in units of the conductance quantum, e^2/h. Blue: Transmission (conductance); Green: Reflection; Red: Total. See text for detailed discussion.
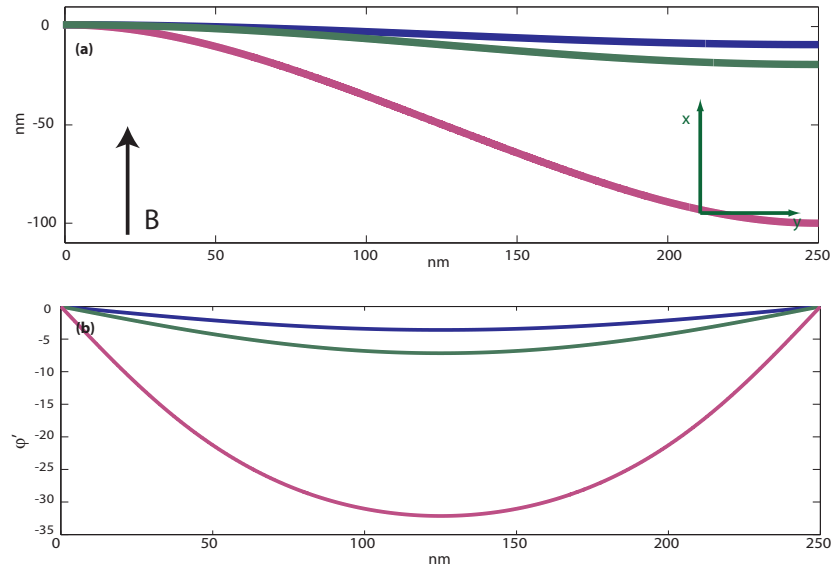
H   Tube geometries

Figure H.1: Relevant geometries for the hill-like tubes. **(a)** Tube bending as a function of the length in the (global) $\hat{y}$-direction. The tubes, listed from top to bottom corresponds to the configurations used in simulations **(b)**-**(d)** in Figure G.2. **(b)** The angle between the starting part of tube and the locally straight tube. Graphs of the same color in **(a)** and **(b)** correspond to the same tube.
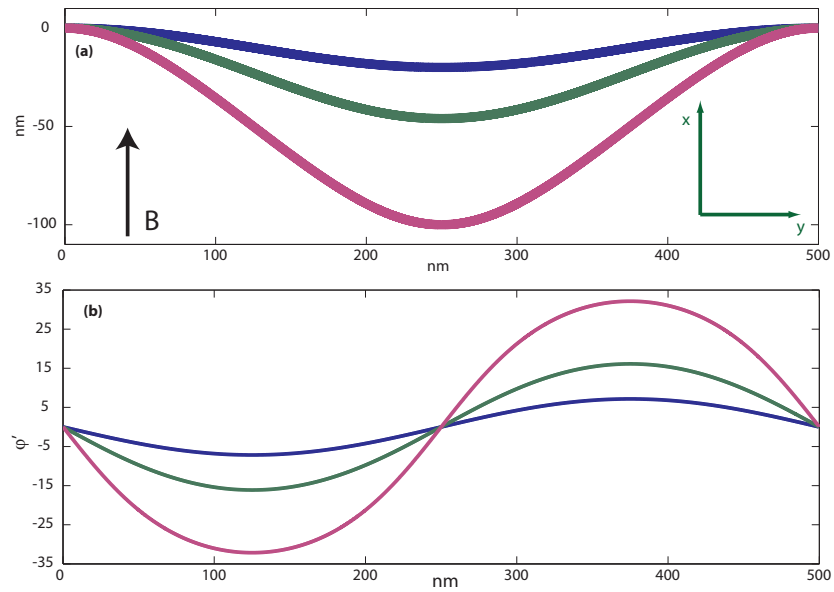

Figure H.2: Relevant geometries for harmonically shaped tubes. **(a)** The tube bending as a function of the length in the (global) $\hat{y}$-direction. The tubes, listed from top to bottom corresponds to the configurations used in simulations **(b)**-**(d)** in Figure G.3. **(b)** The angle between the starting part of tube and the locally straight tube. Graphs of the same color in **(a)** and **(b)** correspond to the same tube.
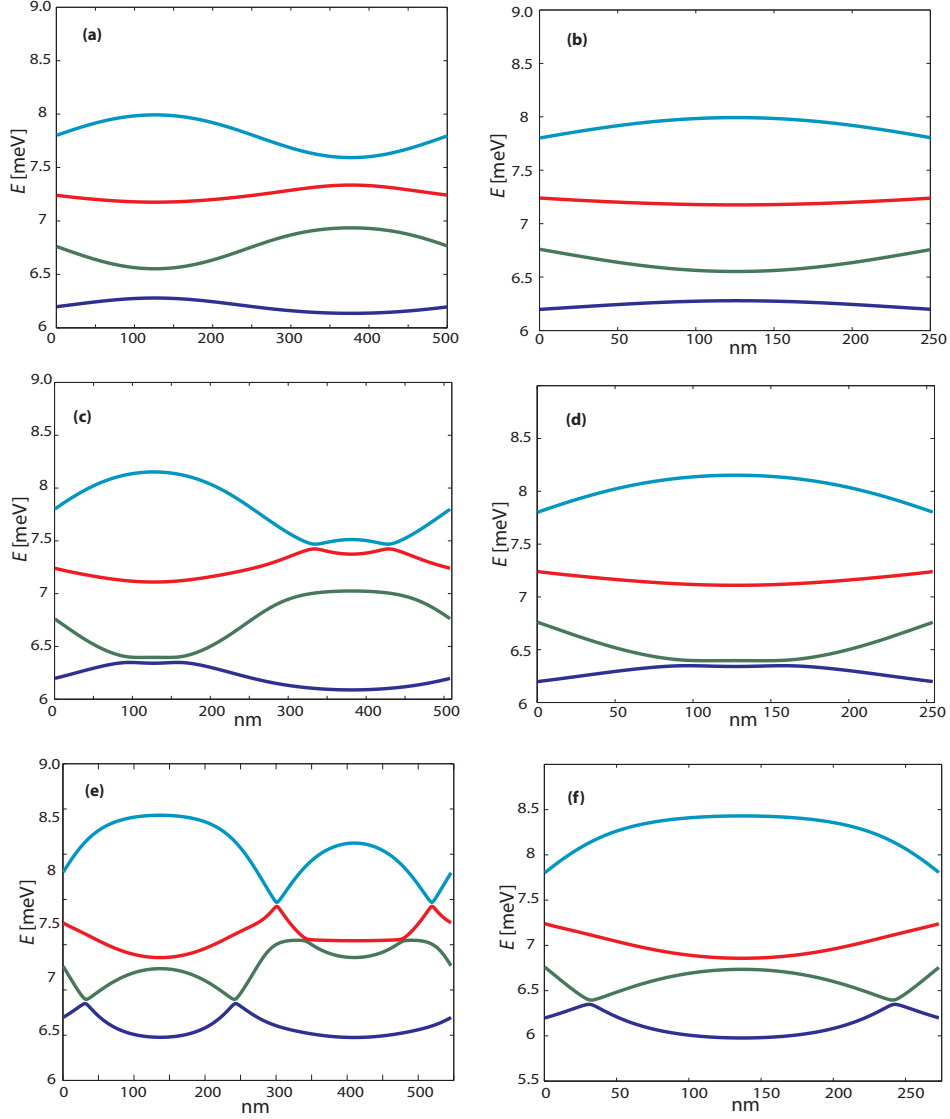
I Potential barriers of bent tubes

Figure I.1: Bottom of the four conduction bands of a metallic zig-zag tube ($\mu = 0$, $\theta = 0$) of radius 2 nm as a function of the location along the tube. **(a)**, **(c)** and **(e)** correspond to the tube geometries depicted in Figure H.2 **(a)**, listed from top to bottom. **(b)**, **(d)** and **(f)** correspond to the tube geometries depicted in Figure H.1 **(a)**, again listed from top to bottom. The size of the potential bumbs are closely related to the geometry of the tube, which is expressed through a varied bend angle.

References

[1] Karsten Flensberg and C. M. Marcus. Bends in nanotubes allow electric spin control and coupling. *arXiv:1003.0037*, 2010.

[2] S. Iijima. Helical Mircrotubules of Graphite Carbon. *Nature*, 354(6348):56–58, 1991.

[3] TW Ebbesen, HJ Lezec, H Hiura, JW Bennett, HF Ghaemi, and T Thio. Electrical conductivity of individual carbon nanotubes. *Nature*, 382(6586):54–56, 1996.

[4] Claire Berger Yan Yi Z. L. Wang and Walt A. de Heer Philippe Poncharal. Room Temperature Ballistic Conduction in Carbon Nanotubes. *The Journal of Physical Chemistry B*, 106 (47), 2002.

[5] F Kuemmeth, S Ilani, D C Ralph, and P L McEuen. Coupling of spin and orbital motion of electrons in carbon nanotubes. *Nature*, 452(7186):448–52, 2008.

[6] Denis V. Bulaev, Björn Trauzettel, and Daniel Loss. Spin-orbit interaction and anomalous spin relaxation in carbon nanotube quantum dots. *Phys. Rev. B*, 77(23):235301, 2008.

[7] B. Lassagne, J.-P. Cleuziou, S. Nanot, W. Escoffier, R. Avriller, S. Roche, L. Forro, B. Raquet, and J.-M. Broto. Aharonov-Bohm conductance modulation in ballistic carbon nanotubes. *Physical Review Letters*, 98(17), 2007.

[8] Daniel Huertas-Hernando, F. Guinea, and Arne Brataas. Spin-orbit coupling in curved graphene, fullerenes, nanotubes, and nanotube caps. *Phys. Rev. B*, 74(15):155426, 2006.

[9] Wataru Izumida, Kentaro Sato, and Riichiro Saito. Spin–orbit interaction in single wall carbon nanotubes: Symmetry adapted tight-binding calculation and effective model analysis. *Journal of the Physical Society of Japan*, 78(7):074707, 2009.

[10] Jae-Seung Jeong and Hyun-Woo Lee. Curvature-enhanced spin-orbit coupling in a carbon nanotube. *Phys. Rev. B*, 80(7):075409, 2009.

[11] MJ Biercuk, N Mason, J Martin, A Yacoby, and CM Marcus. Anomalous conductance quantization in carbon nanotubes. *Phys. Rev. Lett.*, 95(6), 2005.

[12] T Ando. Theory of Electronic States and Transport in Carbon Nanotubes. *Journal of the Physics Society Japan*, 74(3):777–817, 2005.

[13] M. Saito, S.; Dresselhaus, G.; Dresselhaus. *Physical Properties of Carbon Nanotubes*. Imperial College Press, 1. edition edition, 1998.

[14] C. Kittel. *Introduction to Solid State Physics*. John Wiley & Sons Inc., 2005.

[15] M. P. Marder. *Condensed Matter Physics*. John Wiley & Sons, corrected printing edition, 2000.

[16] D. J. Griffith. *Introduction to Quantum Mechanics*. Pearson Education, Inc., 2005.

[17] H. O. H. Churchill, F. Kuemmeth, J. W. Harlow, A. J. Bestwick, E. I. Rashba, K. Flensberg, C. H. Stwertka, T. Taychatanapat, S. K. Watson, and C. M. Marcus. Relaxation and dephasing in a two-electron c13 nanotube double quantum dot. *Phys. Rev. Lett.*, 102(16):166802, 2009.

[18] T Ando and T Seri. Quantum transport in a carbon nanotube in magnetic fields. *Journal of the Physics Society Japan*, 66(11):3558–3565, 1997.

[19] Michael J. Biercuk, Shahal Ilani, Charles M. Marcus, and Paul L. McEuen. Electrical transport in single-wall carbon nanotubes. In *Carbon Nanotubes*, volume 111 of *Topics In Applied Physics*, pages 455–493. Springer-Verlag Berlin, 2008.

[20] A. Urbina, I. Echeverría, A. Pérez-Garrido, A. Díaz-Sánchez, and J. Abellán. Quantum conductance steps in solutions of multiwalled carbon nanotubes. *Phys. Rev. Lett.*, 90(10):106603, 2003.

[21] Pieter Burggraaf. Ballistic conductance observed in carbon nanotubes. *Solid State Technology*, 41(9):34, 1998.

[22] M. F. Lin and Kenneth W. K. Shung. Magnetoconductance of carbon nanotubes. *Phys. Rev. B*, 51(12):7592–7597, 1995.

[23] N.D. Ashcroft, N. W.; Mermin. *Solid State Physics*. Brooks/Cole, third indian edition edition, 2007.